Author Manuscript

Author Manuscript

Author Manuscript

Author Manuscript

HHS Public Access

Author manuscript

*Cell*. Author manuscript; available in PMC 2019 November 29.

Published in final edited form as:

*Cell*. 2018 November 29; 175(6): 1520–1532.e15. doi:10.1016/j.cell.2018.10.043.

# Mechanisms for zinc and proton inhibition of the GluN1/GluN2A NMDA receptor

**Farzad Jalali-Yazdi**[1], **Sandipan Chowdhury**[1], **Craig Yoshioka**[1], and **Eric Gouaux**[1,2,3,*]

[1]Vollum Institute, Oregon Health and Science University, Portland, Oregon 97239, USA

[2]Department of Biomedical Engineering, Oregon Health and Science University, Portland, Oregon 97239, USA

[3]Howard Hughes Medical Institute, Oregon Health and Science University, Portland, Oregon 97239, USA

## Summary

*N*-Methyl-D-aspartate receptors (NMDARs) play essential roles in memory formation, neuronal plasticity and brain development with their dysfunction linked to a range of disorders from ischemia to schizophrenia. Zinc and pH are physiological allosteric modulators of NMDARs with GluN2A containing receptors inhibited by nanomolar concentrations of divalent zinc and by excursions to low pH. Despite the widespread importance of zinc and proton modulation of NMDARs, the molecular mechanism by which these ions modulate receptor activity has proven elusive. Here, we use cryo-electron microscopy to elucidate the structure of the GluN1/GluN2A NMDAR in a large ensemble of conformations under a range of physiologically relevant zinc and proton concentrations. We show how zinc binding to the amino terminal domain elicits structural changes that are transduced though the ligand-binding domain and result in constriction of the ion channel gate.

## In Brief:

CryoEM structures of the full-length GluN1/GluN2A diheteromeric receptor across a range of physiologically relevant zinc and proton concentrations illustrates how zinc binding elicits structural changes that result in constriction of the ion channel gate

## Graphical Abstract

*Correspondence: gouauxe@ohsu.edu.
Lead Contact: Eric Gouaux

Author Contribution

Conceptualization, F.J.Y., S.C., and E.G.; Methodology, F.J.Y. and S.C.; Investigation, F.J.Y. and S.C.; Formal Analysis and Visualization, F.J.Y. and C.Y.; Writing – Original Draft, F.J.Y.; Writing – Review & Editing, F.J.Y. and E.G.; Supervision, E.G.; Funding Acquisition, F.J.Y., S.C., and E.G.

Declaration of Interests

The authors declare no competing interests.

**Publisher's Disclaimer:** This is a PDF file of an unedited manuscript that has been accepted for publication. As a service to our customers we are providing this early version of the manuscript. The manuscript will undergo copyediting, typesetting, and review of the resulting proof before it is published in its final citable form. Please note that during the production process errors may be discovered which could affect the content, and all legal disclaimers that apply to the journal pertain.

Author Manuscript Author Manuscript Author Manuscript Author Manuscript

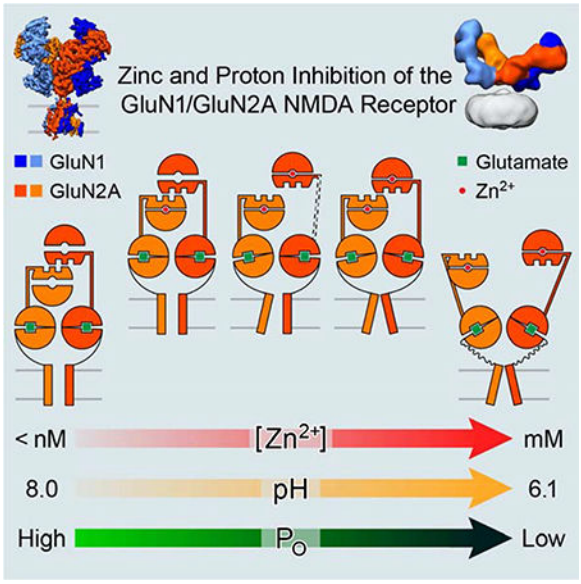


## Introduction

Ionotropic glutamate receptors (iGluRs) mediate fast excitatory neurotransmission in the central nervous system and consist of *N*-methyl-D-aspartate (NMDA), kainate, and AMPA receptors (Traynelis et al., 2010). NMDARs are coincidence detectors whose activation requires the binding of glutamate and glycine and the release of voltage-dependent magnesium block (Nowak et al., 1984). Activation coupled to multiple stimuli, combined with high calcium permeability, underpins the crucial roles of NMDARs in memory formation, the development of long term potentiation, and neuronal plasticity (Bashir et al., 1991; Paoletti et al., 2013). NMDARs are obligate heterotetramers typically consisting of two glycine-binding GluN1 and two glutamate-binding GluN2A-D subunits (Traynelis et al., 2010) which are in turn composed of three major domains: the amino-terminal domain (ATD), the ligand or agonist-binding domain (LBD), and the transmembrane domain (TMD) (Karakas and Furukawa, 2014; Lee et al., 2014). The ATDs and the LBDs have clamshell-like structures and together comprise the extracellular domain (ECD), located in the synapse. Extensive interactions between the ATDs and LBDs allows the ATD to allosterically modulate the function of the receptor (Gielen et al., 2009; Paoletti, 2011).

Zinc, protons, polyamines, and ifenprodil are important allosteric modulators of NMDARs. Within a subset of glutamatergic neurons, most notably within the hippocampus, vesicles containing zinc and glutamate are co-released in an activity-dependent manner (Qian and Noebels, 2005, 2006). Zinc-inhibition of all NMDARs has a voltage-dependent component (Fayyazuddin et al., 2000), similar to the magnesium block at the receptor pore, yet GluN2A-containing NMDARs are inhibited by nanomolar concentrations of zinc in a voltage-independent manner, with a 200-fold greater sensitivity to zinc in comparison to GluN1/GluN2B receptors (Paoletti et al., 1997; Traynelis et al., 1998). Recent studies have uncovered specific evidence for the GluN2A zinc-inhibition in thermosensation,

Author Manuscript Author Manuscript Author Manuscript Author Manuscript

nociception, and in the development and function of the brain (Nozaki et al., 2011; Paoletti et al., 2009; Sensi et al., 2009; Serraz et al., 2016).

Protons also profoundly modulate NMDAR activity. The open-probability ($P_O$) of the receptor is reduced with increasing proton concentration, with a pH $IC_{50}$ value close to physiological pH (Traynelis and Cull-Candy, 1990). Proton-inhibition is strongly coupled to zinc-inhibition. Mutations which increase the sensitivity of the NMDARs to zinc also increase NMDARs' sensitivity to protons (Fayyazuddin et al., 2000; Gielen et al., 2008) and the presence of zinc renders the receptor more susceptible to proton inhibition (Choi and Lipton, 1999; Erreger and Traynelis, 2005, 2008; Gielen et al., 2008; Low et al., 2000; Zheng et al., 2001).

The high affinity zinc site on the GluN2A subunit was first mapped to the ATD (Choi and Lipton, 1999; Fayyazuddin et al., 2000; Low et al., 2000; Paoletti et al., 2000) with subsequent structural studies pin-pointing the site to the GluN2A clamshell cleft (Karakas et al., 2009; Romero-Hernandez et al., 2016). By contrast, elements of the receptor implicated in proton modulation are distributed throughout the receptor, with both the LBD-TMD linkers and the ATD playing a role in pH dependent gating (Gielen et al., 2009; Yuan et al., 2015).

Despite advances in structural and mechanistic studies of NMDARs, the molecular mechanisms to describe zinc and proton inhibition are unresolved. On the one hand, Gielen et al. showed that enhancing the LBD heterodimer stability reduced the extent of proton and zinc-inhibition, whereas disrupting this interface led to more potent inhibition, establishing an important role for the D1-D1 interface in mediating zinc inhibition (Gielen et al., 2008). Exon-5 in the GluN1 subunit attenuates zinc and proton sensitivity of NMDARs by stabilizing the D1-D1 interface, bolstering the notion that the LBD dimer plays an important role in zinc-inhibition (Regan et al., 2018). On the other hand, spectroscopic studies point toward similar zinc and ifenprodil induced movement at the ATD layer (Sirrieh et al., 2013, 2015), while the structures of the NMDA receptor bound to ifenprodil or other phenylethanolamines revealed an intact D1-D1 LBD interface (Tajima et al., 2016; Zhu et al., 2016). Consistent with zinc and ifenprodil inhibiting NMDARs through similar structural mechanisms, ifenprodil enhances zinc and proton sensitivity (Amico-Ruvio et al., 2012; Mott et al., 1998; Pahk and Williams, 1997) and zinc enhances ifenprodil sensitivity and the extent of inhibition (Hansen et al., 2014). Indeed, single molecule studies support an ensemble of electrophysiologically silent states, where the NMDA receptor populates pre-open or low $P_O$ states in the presence of zinc (Amico-Ruvio et al., 2011; Christine and Choi, 1990; Dolino et al., 2017; Erreger and Traynelis, 2008).

Here we solve the first full-length structure of the GluN1/GluN2A diheteromeric receptor and elucidate the structural underpinnings of proton-dependent zinc-inhibition for the GluN2A-containing NMDARs via single-particle cryoEM. We demonstrate closure of the ATD clamshells due to zinc-binding and the transduction of this conformational change through the LBD and finally to the pore. The seven distinct structural conformations observed during the course of this study, some with an intact D1-D1 interface and others with a disrupted D1-D1 interface, illustrate how zinc and proton inhibition leads to a

Author Manuscript Author Manuscript Author Manuscript Author Manuscript

lessening of the tension in the linkers connecting the LBDs to the channel pore, leading to constriction of the ion channel gate.

## Results and Discussion

### Function of the GluN1/GluN2A receptor in membranes and micelles

The GluN1/GluN2A diheteromeric receptor (diNMDAR) construct employed here (see Star*Methods) is sensitive to zinc inhibition, similar to the full length receptor (Figure 1A and Figure S1A-B) (Low et al., 2000; Paoletti et al., 1997). To interrogate zinc modulation of receptor activity in detergent micelles we measured the [$^3$H]MK-801 off rate (Blanke and VanDongen, 2008; Kornhuber et al., 1989; Song et al., 2018) as a function of zinc concentration (Figure 1B). In the presence of saturating zinc, the off-rate of MK-801 is slowed ~2-fold at pH 7.4 compared to the off-rate in the presence of the zinc chelator, tricine (Paoletti et al., 1997). Using a single-site binding model, the off-rate of MK-801 as a function of free-zinc concentration has an $IC_{50}$ of ~20 nM (Figure 1C), similar to the $IC_{50}$ of zinc inhibition measured by electrophysiology, thus showing that the GluN1/GluN2A construct, in detergent micelles, retains zinc modulation of receptor activity.

### Architecture of the GluN1/GluN2A receptor in the absence of zinc

We then elucidated the GluN1/GluN2A receptor structure in the presence of agonists and 1 mM EDTA using single-particle cryoEM (Figure 1D and Figure S2A-C) and modeled the ATD, LBD and TMDs into the density by rigid-body fitting (Figure 1E). The receptor architecture resembles a bouquet (Karakas and Furukawa, 2014; Lee et al., 2014; Lu et al., 2017). Similar to the GluN1/GluN2B receptor (Zhu et al., 2016), the ion channel gate is closed and we speculate that the receptor is a desensitized or preopen conformation. Within the ATD layer, the R2 lobes of opposing GluN2A subunits meet at the pseudo-C2-symmetry axis, with the N-terminus of the α5 helix interacting with the α6 helix of the opposing subunit (Figure 1F and Figure S3). Viewed from ‘above’, the R2 lobes of GluN2A subunits resemble two hands performing a ‘fist bump’, with the α5 and α6 helices representing the “knuckles”. In this “2-knuckle-symmetric” conformation the distance between the COMs of the R1 and R2 lobes are indistinguishable between the two subunits, measured at ~33.6 Å (Figure 1F). Despite overall pseudo-C2-symmetry, there are deviations in conformation between the two GluN2A subunits that include a 13° difference the a ngles between the ATDs and LBDs (Figure 1E; see also Star*Methods), the lengths of the GluN2A LBD-TMD linkers, and the dimer-dimer distances within the LBD layer. Here we employ the ATD-LBD angle to assign chain B (the larger angle) and chain D (the smaller angle) for all of the structures in this study.

### An ensemble of conformations at nanomolar zinc concentration

To elucidate the structural basis for voltage-independent zinc inhibition, we dialyzed the receptor against a buffer containing glutamate, glycine and 1 μM $ZnCl_2$ prior to EM grid preparation. After 3D-classification and refinement, we obtained three separable receptor conformations (Figure S4), structural classes that provide an estimate of the population of conformational states occupied by the receptor in the presence of 1 μM zinc (Figure 2; see also Star*Methods).

Author Manuscript Author Manuscript Author Manuscript Author Manuscript

The “2-knuckle-asym” structure (Figure 1G-H, left) most closely resembles the ‘EDTA’ conformation (Figure 1D), as highlighted by “2-knuckle” interactions between the R2 lobe α5 and α6 helices. There are important differences, however, because in the presence of zinc, the GluN2A ATD ‘clamshell’ of chain B undergoes domain closure by 10.3°, along with a 3° increase in the ATD-LBD angl e. By contrast, the conformational changes in the second GluN2A subunit (chain D) are much smaller and the ATD clamshell adopts a more open conformation, showing that at 1 μM zinc, only one GluN2A ATD undergoes zinc-induced domain closure.

In the second class (Figure 1G-H, middle), deemed the “1-knuckle” conformation, only the opposing α6 helices on GluN2A R2 lobes participate in subunit-subunit interactions. The reduction in ATD-ATD contacts is due to closure of both ATD clamshells and movement of GluN2A R2 lobes COM distances by 5.8 Å. For chain B, the subunit with the larger ATD-LBD angle, the R1 lobe moves by 11.9° to close the ATD clamshell and brings the R1 and R2 lobes closer together by 1.9 Å as compared to the 2-knuckle-sym conformation. Similarly, for chain D, the R1 lobe moves by 15.4° and brings the R1 and R2 COMs closer by 1.8 Å.

In the third class, called the ‘extended’ conformation, one of the ATD heterodimers (chains C and D) moves away from the pseudo symmetry-axis, ablating ATD-ATD interactions between the α5 or α6 helices (Figure 1G-H, right). Both GluN2A ATD clamshells are closed with the R1-R2 COM distance being reduced by ~1.6 Å for each chain with respect to the 2-knuckle-sym conformation. The ‘extended’ ATD heterodimer (chains C and D) shows more diffuse density as compared to the rest of the ECD, suggestive of conformational heterogeneity.

### Conformations of the GluN1/GluN2A/GluN2A* triheteromeric receptor

To investigate whether the closed and open ATD ‘clamshells’ in the 1 μM “2-knuckle-asym” conformation are the consequence of zinc-bound and zinc-unbound states, respectively, and to probe the extent to which conformational changes are propagated throughout the receptor, we carried out cryoEM studies on a ‘triheteromeric’ GluN1/GluN2A/GluN2A* receptor where the GluN2A* subunit harbors a His 128 to Ser mutation (Figure S3). This substitution, at the high affinity GluN2A ATD zinc site, decreases zinc potency by ~500-fold and reduces the extent of zinc inhibition (Fayyazuddin et al., 2000; Hansen et al., 2014; Hatton and Paoletti, 2005; Paoletti et al., 2000). We selectively isolated the ‘triheteromeric’ receptor by 2-step affinity chromatography and distinguished the GluN2A and GluN2A* subunits in cryoEM density maps by knocking out a prominent glycosylation site (N687) in the LBD layer of the GluN2A* subunit (Figure S3).

We first solved the structure of the GluN1/GluN2A/GluN2A* triheteromeric receptor (triNMDAR) in the presence of agonists and 1 mM EDTA. This structure (Figure 3A and Figure S2D-F) is similar to the 2-knuckle-sym conformation of the GluN1/GluN2A diNMDAR. For the triNMDAR in the absence of zinc, we do not observe a signal consistent with glycosylation at either subunit, whereas for the diNMDAR the glycosylation density is substantial for both subunits (Figure 3B-C). The lack of glycosylation density in the triNMDAR reconstruction is due to the averaging of the density for the GluN2A and

Author Manuscript Author Manuscript Author Manuscript Author Manuscript

GluN2A* subunits because both subunits adopt similar conformations in the absence of zinc.

In the presence of 1 μM zinc, however, the triNMDAR occupies four previously observed conformations (Figure 3D and Figure S5). Interestingly, compared to the diNMDAR, the triNMDAR particles occupied a larger fraction in the 2-knuckle classes than the 1-knuckle conformation (Figure 2). The 2-knuckle-asym class incorporates the most particles and presents a clear distinction between the GluN2A (chain B) and GluN2A* (chain D) subunits based on the glycosylation 'marker' at N687 (Figure 3E). Here, chain B adopts a closed ATD clamshell conformation with a larger ATD-LBD angle, and chain D adopts an open clamshell conformation. We next rigid-body fit the xray structure of the GluN2A ATD – zinc complex (Romero-Hernandez et al., 2016) into R1 lobe densities for the GluN2A and GluN2A* subunits. In GluN2A subunit chain B, there is density associated with the zinc-binding pocket (Figure 3F, top) which has a tetrahedral shape and is consistent with zinc coordinated by sidechains of H44, H128, E266, and D282. By contrast, there is no density around the zinc site when the x-ray derived ATD model is fit into the density for chain D, consistent with the GluN2A* subunit lacking a high affinity zinc site (Figure 3F, bottom). We emphasize that this triNMDAR 2-knuckle-asym cryoEM map and resulting structure, which represents the highest resolution map obtained in this study (Figure S1C-L), confirms that the 2-knuckle-asym class represents dimorphic GluN2A ATDs, with one in the open, apo zinc state and the other in the closed, zinc bound conformation.

The triNMDAR 1-knuckle and extended conformations have the ATD clamshells in the closed conformations, even though one subunit lacks the high-affinity zinc-binding site. It is unlikely that the closed ATD clamshells in the 1-knuckle and extended conformations represent a GluN2A diheteromeric "contaminant" in the triNMDAR sample, as the density for glycosylation at N687 is absent in chain D of the 1-knuckle structure, and in both chains of the extended structure. Most importantly, the closed ATD clamshells of both subunits in these structures is consistent with the notion that the conformational changes from zinc binding to one subunit can propagate throughout the receptor and induce conformational changes in other subunits, even if, for example, the other subunit lacks a high-affinity zinc-binding site.

## Conformational changes due to proton and millimolar zinc concentration

Electrophysiology experiments show that the extent of zinc inhibition is ~98% at pH 6.2 (Figure S1B). To understand how protons enhance the extent of zinc inhibition, we prepared the GluN1/GluN2A receptor in a MES buffer at pH 6.1 in the presence of agonists and 1 μM zinc. Analysis of 2D class averages shows a number of 2D classes with the ATD dimers farther apart than observed previously (Figure 4A). After 3D-classification (Figure S6A-B), we obtained a structural class where the two dimers have lost the ATD-LBD domain swap and show a 'super splayed-open' conformation (Figure 4B right, and Figure S6I-J). The splayed conformation also shows a disruption of the D1-D1 interface within the LBD dimers. In addition to the super-splayed class, we also obtained the 1-knuckle and the extended conformations (Figure 4B and Figure S6C-H).

Author Manuscript Author Manuscript Author Manuscript Author Manuscript

In contrast to the receptor at pH 7.4 in the presence of 1 μM zinc, at pH 6.1 and with 1 μM zinc we do not observe any classes in the 2-knuckle-asym conformation (Figure 2). This "shift" of the structural populations away from the 2-knuckle-asym conformation is consistent with electrophysiological studies showing protons sensitize the receptor to zinc-inhibition, as well as zinc and proton inhibitions being strongly coupled to each other (Erreger and Traynelis, 2005; Low et al., 2000; Zheng et al., 2001). While there is evidence that the proton sensors on the receptor are distributed through various domains, Yuan et al. have proposed Glu106 in the R1 lobe and Glu235 in the R2 lobe as the proton sensors in the ATD of the GluN2B, forming carboxylic acid "dimers" at low pH values when one or both sidechains are protonated (Yuan et al., 2015), leading to the stabilization of the closed ATD clamshell conformation. The corresponding residues in the GluN2A subunit are Glu107 and Asp234. These residues are positioned such that their α-carbon atoms move closer by ~3 Å in the closed clamshell conformation, allowing for the formation of the carboxylic acid "dimer". Given the limited resolution of the present studies, we are not able to conclusively visualize this interaction. Nevertheless, we speculate that at high pH, GluN2A Glu107 and Asp234 are deprotonated and repel one another, stabilizing the clamshells in open cleft conformations. As proposed by Yuan et al., at lower pH values, protons bind to one or both carboxylates, allowing for formation of favorable carboxylic acid 'dimers' and stabilizing the clamshell in a closed cleft conformation (Yuan et al., 2015). Because zinc and protons stabilize the GluN2A ATD clamshells in closed cleft conformations yet by way of different mechanisms, we can understand how zinc and protons act synergistically.

As a counterpoint to decreasing the pH to obtain maximal zinc-inhibition, we examined the structure of the receptor at high pH in the presence or absence of zinc to assess conformational changes leading to minimal zinc-inhibition. We acquired data sets of the GluN1/GluN2A receptor at pH 8.0 in 0.1 mM EDTA, or at pH 8.0 and 1 μM zinc (Figure S2J-O). Both datasets yielded only the 2-knuckle-sym conformation after 3D-classification (Figure 2).

We next examined the conformations of the receptor in the presence of 1 mM zinc at pH 7.4. The voltage-independent component of zinc-inhibition plateaus at ~1 μM zinc, and further increasing the zinc concentration does not lead to more voltage-independent inhibition (Paoletti et al., 1997). There exist, however, additional zinc-binding sites on GluN1 and GluN2B ATDs (Karakas et al., 2009; Romero-Hernandez et al., 2016), and we were interested to learn if there are distinct structural classes associated with high zinc concentrations. Indeed, there are glutamatergic neurons with millimolar zinc concentrations inside presynaptic vesicles (Sensi et al., 2009) and upon release synaptic zinc concentrations can rise above 100 μM (Vergnano et al., 2014).

We acquired a dataset with the GluN1/GluN2A receptor at pH 7.4 in the presence of agonists and 1 mM zinc. Inspection of micrographs and 2D-class averages show that many receptor particles have splayed-open conformations, with their ATD dimers far away from each other (Figure 4C). After 3D-classification, three distinct classes emerged (Figure 4D and Figure S7). The most populated class (Figure 2) shows similar structural elements to the extended conformation, and was named the extended-2 class.

Author Manuscript Author Manuscript Author Manuscript Author Manuscript

The second class we encountered at 1 mM zinc concentration shows a disrupted D1-D1 interface at the LBD dimers with moderately separated ATD heterodimers, and was thus labeled the splayed-open class. While this class originally accounted for ~16% of the 2D-cleaned up particles, the resolution of the class was improved by subsequent rounds of 3D-classification and refinement. This class represents the highest resolution structure of the NMDA receptor in a conformation with a disrupted D1-D1 interface. The final class that we observed shows a similar conformation to the super-splayed class seen in the low-pH dataset.

To confirm that the conformations in the presence of 1 mM zinc do not represent irreversibly unfolded receptor due to the millimolar zinc concentrations, after the initial grids were frozen with 1 mM zinc we added 3 mM EDTA to the remainder of the sample and prepared cryoEM grids. Remarkably, 3D-classification and refinement led only to the 2-knuckle-sym conformation (Figure S2G-I). These results are consistent with the splayed-open or the super-splayed conformations being in reversible equilibrium with the more ‘compact’ 2-knuckle conformations.

When we analyzed the D1-D1 separation of the LBD dimer for all structures, we did not observe any classes other than the splayed-open and super-splayed where the D1-D1 interface was substantially altered (Figure 4E). Interestingly, the super-splayed conformation has been observed before in the context of competitive antagonist complexes of the GluN1/GluN2B NMDAR (Zhu et al., 2016). One of the characteristics of GluN1/GluN2B splayed classes was the clockwise rotation of the GluN2B LBD clamshells by 92–118°. For the GluN2A LBDs, we obse rved a 45–49° clockwise rotation in our splayed-open class, and a 79–98° rotation in the super-splayed class as compared to the extended-2 conformation (Figure 4F).

## Zinc-induced conformational rearrangements at the ATD

The GluN2A clamshell undergoes closure upon zinc-binding. To identify closed vs open ATD clamshells, we measured the R1-R2 COM distance for the two GluN2A subunits. The 2-knuckle-sym conformation has both ATD clamshells in the open state, while the 1-knuckle, extended, and extended-2 conformations represent both ATD clamshells in the closed state (Figure 5A). The 2-knucle-asym conformation has one clamshell in the open position (chain B) and the other clamshell (chain D) in the closed positon.

The R2 lobes of GluN1 and GluN2A ATD play a critical role in transduction of ATD conformational changes to the LBD, as they are directly connected to the LBD D1 lobes. Upon zinc- and proton-induced closure of the GluN2A ATD clamshell, the R2 lobes of GluN1 and GluN2A within each ATD heterodimer move apart by ~3 Å (Figure 5B). Chain D of the extended conformation experiences an additional 1.4 Å expansion ($p = 0.01$) when the ATD heterodimer extends from the receptor and loses interaction with the LBD layer. The separation of the ATD heterodimer R2 lobes has been implicated in the negative allosteric modulation of NMDARs by electrophysiology (Mony et al., 2011), and has been observed in the inhibition of the GluN2B containing receptors by phenylethanolamines (Tajima et al., 2016; Zhu et al., 2016).

Author Manuscript Author Manuscript Author Manuscript Author Manuscript

Movement of the R2 lobes of GluN2A subunits at the pseudo-symmetry axis is also associated with zinc and proton inhibition of the receptor. In all classes with an intact D1-D1 interface at the LBD dimer, the R2 lobes of GluN2A move perpendicular to the R1-R2 axis, resulting in lateral movement of the lobes away from each other and the formation of the 1-knuckle and extended conformations (Figure 5C). This lateral R2-R2 movement is only observed in conformations with both ATD clamshells in closed conformations.

## Transduction of conformation changes from the ATD to the LBD

To understand how conformational changes within the ATD layer are transduced to the LBD layer, we first examined the ATD-LBD angle (see Star*Methods). When the ATD clamshell of chain B adopts a closed conformation as in the 2-knuckle-asym conformation, the ATD-LBD angle increases by ~6° in comparison to the 2-knuckle sym conformation (Figure 6A). In contrast, the ATD-LBD angle remains unchanged for chain D, which does not undergo ATD clamshell closure. In the 1-knuckle conformation, where both ATD clamshells are closed, there is a 12° increase in the chain D ATD-LBD angle and a 6° increase for chain B as compared to the 2-knuckle-sym state. In the case of chain D of the extended conformation, there is no correlation between the ATD clamshell conformation and the ATD-LBD angle simply because the entire ATD no longer interacts with other domains of the receptor.

To understand how the ATD-LBD linkers participate in transducing conformational changes between the ATD and LBD layers (Gielen et al., 2009), we examined the distance between the COMs of the R2 lobe of the ATD to the D1 lobe of the LBD (Figure 6B). For the 2-knuckle-asym and the 1-knuckle conformations, the difference between R2-D1 COM distances as compared to the 2-knuckle-sym conformation is ≤ 0.6 Å. The movement away from the pseudo-C2-symmetry axis of chain D in the extended conformation increases the R2-D1 distance in this chain by 6.1 Å. Indeed, the cryoEM density for the ATD-LBD linkers in GluN2A are well-resolved in the 2-knuckle and 1-knuckle structures, yet it is non-existent in the ATD heterodimer that is displaced from the pseudo symmetry axis in the extended conformation of the receptor. We speculate that the well-ordered, defined structure of the ATD-LBD linkers in GluN2A allows the movements of the ATD R2 lobes to be directly translated to the LBD for the 2-knuckle and 1-knuckle conformations. For the extended conformation, however, the linker on chain D is extended and disordered, uncoupling the ATD heterodimer from the receptor.

Propagation of conformational changes from the ATD layer to the LBD layer also occurs by the lateral movement of the ATD R2 lobes at the pseudo-symmetry axis (Figure 5C) ‘pushing’ the opposing D1 lobes of GluN2A directly away from each other and bringing the D2 lobes closer together. To quantify the LBD movement, we connected the COMs of the opposing D2 lobes of GluN2A with a vector. The angle that this vector makes with vectors passing through the COMs of the D2 and D1 lobes of chains B and D are labeled δ and ε respectively (Figure 6C). Movement of the opposing D1 lobes away from each other while the D2 lobes come closer increases both δ and ε. The values for δ and ε are indistinguishable between the two 2-knuckle conformations, consistent with observations that the closure of a single ATD clamshell does not result in the lateral movement of R2-

Author Manuscript Author Manuscript Author Manuscript Author Manuscript

lobes. However, there is a ~7.4° increase in both δ and ε for the 1-knuckle conformation as compared to the 2-knuckle-sym conformation. While ε remains similar between the 1-knuckle and extended conformations, δ decreases by ~2.3° ($p = 0.005$). Both δ and ε are further decreased in the extended-2 conformation. The decrease in δ and ε when comparing the 1-knuckle state to the extended states is consistent with the less efficient transfer of the zinc-induced conformational changes at the ATD to the LBD for the extended conformations. In the splayed conformations, δ and ε increase by >30° as the D1 lobes moved far away fr om each other.

## Channeling inhibition to the pore

How are changes at the ATD and LBD layers conveyed to the pore? Helix E in the D2 lobe of the LBD is directly connected to the M3 helix. The M3 helices, in turn, form the ion channel gate. We measured the distance between the E helices of the GluN2A subunits. We speculate that the larger the helix E separation, the greater the tension on the M3 helices and the higher probability of finding the gate in an open conformation. The rocking motion of LBDs upon zinc binding (Figure 6D) brings the D2 lobes closer together, resulting in the reduction of opposing helix E separation. This distance remains similar in the two 2-knuckle conformations and is reduced by 3.2 Å and 2.5 Å in the 1-knuckle and extended conformations, respectively. The opposing helix E distance is similar in the 2-knuckle states and the extended-2 state, and this distance is reduced substantially (23 Å – 56 Å) in the splayed and super-splayed conformations. Consistent with the LBD rocking motion (Figure 6C), where the effects of zinc binding at the ATD was transferred to the LBD with lower efficiency for the extended and extended-2 conformations, the helix E separation in these conformations is also larger than the 1-knuckle conformation. The larger helix E separation for the extended and extended-2 conformations will likely result in a higher $P_O$ for these states as compared to the 1-knuckle state. The splayed open conformations show the lowest helix E separation, consistent with these classes having a $P_O$ value close to zero.

We also measured the distance between the COM of residues 4–7 of the lurcher motif (SYTANLAAF) (Zuo et al., 1997) in GluN1 (Figure S1M) or GluN2A (Figure S1N) subunits to define the conformation of the ion channel gate. While do not believe that any of the structures reported here show gate in a fully-open conformation, such as that found in molecular dynamics simulations (Song et al., 2018), we do observe a reduction in the distances between the M3 helices at the ion channel gate in the 2-knuckle states and the 1-knuckle state for both GluN1 (1.3 Å) and GluN2A (2.1 Å) subunits. Consistent with the previous LBD and TMD observations, the M3 separation is similar between the two 2-knuckle states.

## Mechanism

We propose the following mechanism for zinc and proton inhibition of the GluN1/GluN2A NMDARs (Figure 7). At high pH, in presence of agonists and EDTA, the receptor populates the ‘2-knuckle-sym’ conformation with GluN2A ATDs in open clamshell conformations and the R2 lobes of opposing GluN2A subunits positioned back-to-back on the pseudo-C2 symmetry axis. At lower pH values and upon binding zinc, the receptor progressively populates greater fractions of the 2-knuckle-asym, 1-knuckle, extended, extended-2,

Author Manuscript Author Manuscript Author Manuscript Author Manuscript

splayed-open and super-splayed conformations (Figure 2). When the receptor transitions from the 2-knuckle-sym to the 2-knuckle-asym conformation, one GluN2A subunit undergoes ATD clamshell closure while the other ATD clamshell remains open. The closure of a single ATD clamshell is not sufficient to move the R2 lobes of GluN2A from their original back-to-back position at the pseudo-symmetry axis, and leads only to minor structural changes within the LBD layer and no discernable conformational changes in the LBD-TMD linkers. However, closure of both ATD clamshells moves the R2-lobes of GluN2A away from each other and results in a rocking-like movement of the GluN2A LBD clamshells, causing the opposing D1 lobes to move away from each other and bringing the D2-lobes closer together, relieving tension in the LBD-TMD linkers. Under conditions of low pH and micromolar concentrations of zinc, the receptor adopts splayed-open and super-splayed conformations where the LBD D1-D1 interface is disrupted, leading to a large rocking motion of the LBD dimers and entirely releasing tension on the LBD-TMD linkers.

Based on the LBD rocking movements (Figure 6C), helix E/helix E separation (Figure 6D), and the gate diameter measurements (Figure S1M-N), we speculate that the two 2-knuckle states are functionally equivalent, and represent the receptor in the highest $P_O$ states. The extended and extended-2 conformations represent the next highest $P_O$ states. Surprisingly, based on the LBD measurements, the extended-2 conformation should exhibit a similar $P_O$ to the 2-knuckle states. The 1-knuckle and splayed conformations represent the lowest $P_O$.

Our findings provide a structural justification for why we observe a higher degree of zinc-inhibition at low pH values, as we did not observe any classes with the 2-knuckle or extended-2 conformations under these conditions and all of the particles were in the lower $P_O$ conformations. Similarly, we did not observe any classes other than the 2knuckle conformations for the receptor at pH 8.0, representing higher $P_O$. We can also explain why at 1 mM zinc, when we observe a large portion of the particles in the splayed conformations, we do not observe a larger degree of voltage-independent zinc-inhibition by electrophysiology (Paoletti et al., 1997). Even though at 1 mM zinc, ~31% of the particles are in the splayed conformations, ~46% of the particles are in the extended-2 conformation, representing high $P_O$. Finally, we can account for the lower level of zinc-inhibition in the GluN1A/GluN2A/GluN2A* triNMDAR vs. the diNMDAR, as >50% of particles in the triNMDARs are in the 2-knuckle states vs. <20% for the diNMDARs (Figure 2). We were also able to demonstrate the reversibility of splayed and super-splayed conformation, and demonstrated that with the removal of zinc the receptor reverts back to the 2-knuckle-sym conformation.

Here we show how the GluN1/GluN2A receptor populates an ensemble of structural states depending on zinc and proton concentrations (Amico-Ruvio et al., 2011; Dolino et al., 2017; Erreger and Traynelis, 2008). The 1-knuckle conformation, one of the structural conformations that the receptor adopts when inhibited by zinc and protons, resembles the GluN1/GluN2B receptor bound by ifenprodil or Ro25–6891 (Tajima et al., 2016; Zhu et al., 2016). The ‘splayed’ conformations, structural states populated at high concentrations of zinc or protons, display disrupted D1-D1 interfaces at the LBD dimer and are reminiscent of competitive antagonist-bound states of the GluN1/GluN2B receptor (Zhu et al., 2016). Thus, our findings reconcile how zinc and proton modulation of GluN2A receptor activity shares

Author Manuscript Author Manuscript Author Manuscript Author Manuscript

mechanistic elements of ifenprodil inhibition of GluN2B receptors via conformational changes in the ATD layer (Sirrieh et al., 2015) and also with mechanisms involving the disruption of the D1-D1 interface within the LBD layer (Gielen et al., 2008; Regan et al., 2018). While we are unable to pinpoint the proton sensors of the GluN1/GluN2A receptor, our observations are consistent with the proposal that zinc sensitizes the receptor to proton inhibition (Choi and Lipton, 1999; Erreger and Traynelis, 2008; Gielen et al., 2008; Low et al., 2000). In line with this mechanism, in the presence of 1 μM zinc when the proton concentration is increased from pH 7.4 to pH 6.1, the structural populations shift resulting in the receptor no longer occupying the 2-knuckle-asym conformation, and when the proton concentration is decreased to pH 8.0 the receptor only occupies the 2-knuckle-sym conformation. Furthermore, by solving the structure of the GluN1/GluN2A/GluN2A* triheteromeric receptor in the presence of zinc, we show how subunit-specific conformational changes can be both localized to specific subunits yet also propagated throughout the entire receptor.

## Star*Methods

### CONTACT FOR REAGENT AND RESOURCE SHARING

Requests for reagents may be directed to the Lead Contact Eric Gouaux (gouauxe@ohsu.edu).

### EXPERIMENTAL MODEL AND SUBJECT DETAILS

**Cell lines—**SF9 cells (ATCC CRL-1711) were cultured in Sf-900 III SFM (ThermoFisher Scientific) at 27 °C. These cells were used for exp ression of Baculovirus, and are female in origin. TSA201 cells (RRID: CVCL_2737) were cultured in FreeStyle 293 Expression Medium (Sigma) at 37 °C supplemented wit h 2% (v/v) fetal bovine serum. These cells are female in origin. Unfertilized *Xenopus laevis* oocytes were purchased from Ecocyte Biosciences, and kept at 18 °C until i njection.

### METHOD DETAILS

**Construct Design:** DNA for the first 847 residues of the *rattus norvegicus* Grin1–1a (P35439–1) and the first 866 residues of Grin2A (G3V9C5) was cloned into Bacmam expression vectors (Goehring et al., 2014). Both genes contain a thrombin cut site (LVPRGS), a four-alanine flexible linker, and an EGFP-tag on their C-terminus, with an 8XHIS-tag on the GluN1 vector and a Strep-tag II on the GluN2A vector, following EGFP. These constructs are referred to as $N1_{EM}$ and $N2A_{EM}$. A bicistronic plasmid of $N1_{EM}$/$N2A_{EM}$ was constructed to express the diheteromeric GluN1/GluN2A NMDAR (diNMDAR). For the triheteromeric receptor (triNMDAR), the $N1_{EM}$ plasmid was modified by the removal of the 8XHIS-tag ($N1_{EMNoHIS}$). A version of $N2A_{EM}$ was constructed with an 8XHIS-tag replacing the Strep-tag II ($N2A_{EMHIS}$). Finally, another version of the $N2A_{EM}$ was constructed with an H128S mutation, as well as an N687Q mutation ($N2A_{EM*}$). A bicistronic construct of $N2A_{EMHIS}$/$N2A_{EM*}$ was created, and co-transfected with $N1_{EMNoHIS}$ into tsa201 cells to express the triNMDAR. For radiolabeled functional assays, the $N2A_{EM}$'s Strep-tag II was exchanged for a high-affinity streptavidin binding peptide tag

Author Manuscript Author Manuscript Author Manuscript Author Manuscript

(DNSA-tag, AA sequence: WIDFNRWHPQSGLPPPPILR, Takahashi et. al, manuscript in preparation).

**Protein Constructs, Expression, Purification—**Baculovirus was generated in sf9 insect cells, and P2 virus was used to infect tsa201 cells at a multiplicity of infection (MOI) of 1:1. The receptors were purified as previously reported (Zhao et al., 2016; Zhu et al., 2016). In brief, at 10 hours post-infection, 10 mM sodium butyrate, alongside either 100 μM of memantine-HCl or 10 nM MK-801 (only in the case of protein used for pH 8.0 datasets) were added to the culture and the flasks were shifted to 30 °C. Cells were sp un and harvested between 36–48 hours post infection and washed in 1X TBS (150 mM NaCl, 20 mM Tris-HCl, pH 8.0). Cells were resuspended using 1 mL of resuspension buffer (1X TBS supplemented with 2 mM PMSF, 1.6 μM aprotinin, 4 μg/mL leupeptin, and 4 mM pepstatin A) per 1 g of cell pellet and manually pipetted until no clumps remained. Equal volume of lysis buffer (1X TBS supplemented with 2% digitonin, 1 mM Cholesteryl Hemisuccinate, 1 mM PMSF, 0.8 μM aprotinin, 2 μg/mL leupeptin, and 2 mM pepstatin A) was added to the mixture, and the sample was agitated by nutation or using a magnetic stirrer for 90 minutes at 4 °C. The mixture was then spun for 1 hour at 185k rc f, and the supernatant was filtered through a 0.2 μm filter to remove debris. The supernatant was then bound to streptactin resin, washed with 10× column volume of WBI (1X TBS supplemented with 0.1% digitonin, 2 mM ATP, 2 mM $MgCl_2$), 10× column volume of WBII (1X TBS supplemented with 0.1% digitonin), and eluted in WBII supplemented with 5 mM desthiobiotin. The receptor was concentrated and further purified using size-exclusion chromatography (SEC) using a buffer containing 150 mM NaCl and the appropriate buffering agent (20 mM Tris at pH 8.0, 20 mM HEPES at pH 7.4, or 20 mM MES at pH 6.1). Peak fractions were combined, concentrated, and used for further experiments.

For the triheteromeric construct, after streptactin purification (Strep-tag II on the GluN2A* subunit), 10 mM imidazole was added to the elution, and the sample was bound to Talon resin for HIS-tag purification (HIS-tag on the wt-GluN2A subunit). The column was washed with 10  column volume of WBII supplemented with 10 mM imidazole. The protein was eluted from the Talon resin using 300 mM imidazole in WBII. The elution fractions were combined, concentrated, and SEC purified as described above.

For the structural experiments of the receptor in the absence of zinc, 0.1 – 3 mM EDTA was used to chelate any zinc contaminations introduced either during the purification of the receptor, or during the blotting step of the cryoEM sample preparation.

**Two Electrode Voltage Clamp Electrophysiology—**The $N1_{EM}$ and $N2A_{EM}$ constructs were subcloned in pGEM vector and *in vitro* transcribed to generate mRNAs. *Xenopus laevis* oocytes were injected with 0.5 ng total mRNA (equal amounts of N1 and N2A) and after 12 – 24 hrs of incubation at 18 °C currents were measured using two-electrode voltage clamp (Axoclamp 200B) at a holding voltage of −60 mV. The base recording solution was (in mM): 60 NaCl, 40 HEPES, 10 Tricine, buffered initially to pH 10.3 and then re-buffered to different pH using HCl. Zinc was added from a 100 mM stock of $ZnCl_2$ and free-zinc was estimated as: $[Zn]_{total}/200$ (Gielen et al., 2008). Recordings were carried out in triplicates. Data was analyzed using MATLAB.

Author Manuscript Author Manuscript Author Manuscript Author Manuscript

**Scintillation Proximity Assay (SPA)—**SPA assays were set up using 40 nM purified protein in 1X HBS (pH 7.4) supplemented with 0.1% digitonin, 10 mM tricine, 0.5 mg/mL of YSi-streptavidin beads, and 100 nM [$^3$H]MK-801 per well. Various additives such as 100 μM glutamate/glycine, and $ZnCl_2$ were added to the wells, but the final volume was kept at 100 μL. Samples were run in triplicates. Concentration of free zinc was estimated as described above. The plate was placed inside a microbeta TriLux 1450 LSC plate reader and read every 12 minutes. After allowing 12 hours for [$^3$H]MK-801 to reach equilibrium, 100 μM non-labeled MK-801 was added to each sample to prevent the re-binding of radiolabeled ligand, and the plate was placed back in the plate reader to measure the off-rate of MK801. Data was analyzed using a one-site binding model.

**CryoEM Sample Preparation/Image Acquisition—**SEC purified protein was used for cryoEM sample preparation. QUANTIFOIL AU 1.2/1.3 300 mesh grids were glow discharged for 1 minute at 15 mA with the carbon side facing up. For all conditions, 1 mM glutamate and glycine were added to the samples. For low zinc concentration samples (1 μM), concentrated protein was placed in a dialysis bag (heavy-metal free Dispodialyzer) and dialyzed against 2000× volume of a buffered solution containing 0.1% digitonin, 1 mM glutamate/glycine and 1 μM $ZnCl_2$. The sample was dialyzed for a minimum of 4 hours and then used for grid preparation. Vitreous sample was prepared by applying 3–4 μL of protein solution at ~4 mg/mL, blotting the excess solution away for 3 seconds using the FEI Vitrobot at 18 °C and 100% humidity, and plunge-freezing the grid in liquid ethane.

For all of the datasets except for the diheteromeric receptor at pH 7.4 with 1 mM EDTA, data collection was carried out at Oregon Health and Science University Multiscale Microscopy Core using a 300 kV FEI Titan Krios equipped with an energy filter (Gatan Image Filter). Images were collected using a Gatan K2 direct electron detector in super-resolution mode at 81kx magnification (unbinned pixel size of 0.855 Å/pixel). Images were collected using serialEM (Mastronarde, 2005) with a typical defocus range of −1 – −2.5 μm and with a total dose of ~55 $e^-/Å^2$. The diheteromeric receptor at pH 7.4 with 1 mM EDTA dataset was collected at the Howard Hughes Medical Institute's CryoEM Facility at the Janelia Research Campus, using an FEI Titan Krios equipped with a Cs corrector and an energy filter (Gatan Image Filter). This dataset was collected using the super resolution mode on a K2 direct electron detector in super-resolution mode with an unbinned pixel size of 0.66 Å/pixel.

**Data Processing, Classification, Refinement—**Image stacks were aligned to compensate for motion during recording and dose- weighted to compensate for radiation damage using MotionCor2 (Zheng et al., 2017), Fourier space binned 2 × 2, and the contrast transfer function was estimated using Gctf (Zhang, 2016). Template-free automatic particle selection was done using DoG-Picker (Voss et al., 2009) or gAutomatch (Unpublished: URL http://www.mrc-lmb.cam.ac.uk/kzhang/Gautomatch/). Reference-free 2D-classification of particles was carried out in RELION (Fernandez-Leiro and Scheres, 2017; Scheres, 2012) followed by manual inspection, selection of the classes representing NMDARs, and further classification. Generally, three rounds of 2D-classification were performed with binned particles (initial round with particles binned by 5, subsequently binned by 3, followed by the

Author Manuscript Author Manuscript Author Manuscript Author Manuscript

last round without binning). After each round, particles were re-centered and re-extracted with the new binning factor. After 2D-cleanup of reference free picked particles, ~30 of the 2D class averages, representing a diverse set of projections, were used for template-based particle picking by gAutomatch. This set of particles was also cleaned up through three rounds of 2D-classification as described above. The two cleaned up particle sets (template-free and template-based) were then combined, and duplicate particles were removed by eliminating any particle whose center was closer than 90 Å to another particle. This combined dataset was then used in 3D-classification and refinement.

The initial model for classification was *de novo* generated using CryoSPARC (Punjani et al., 2017). This model was then used in RELION for 3D-classification. Focused classification (focusing on ECD) was used in the datasets to better separate classes with similar structural features. Some datasets were classified into different number of classes (i.e. 9, 7, and 5), and the classes with the same structural conformations were combined, and duplicate particles removed. After additional rounds of refinement/further classification, the final particle set for each class was exported to cisTEM (Grant et al., 2018). Further refinement in cisTEM was carried out by masking out the micelle, while keeping the TMD of the receptors for alignment. The area outside of the mask was filtered to 20 Å and down-weighted for alignment. For a more accurate and conservative resolution estimate, the cisTEM-generated half-maps were used in RELION to generate the Fourier Shell Coefficient (FSC) curve, and the resolution was calculated at FSC = 0.143 (Scheres and Chen, 2012). Local resolution estimations were generated using Bsoft (Heymann et al., 2008). For a higher resolution reconstruction of the 2 knuckle asym class of the triNMDAR, a focused refinement based on an ECD mask was performed. The resolution of the final reconstruction was improved by ~0.5 Å. The final maps were sharpened by Phenix.Autosharpen (V1.13) using the resolution of the map obtained from cisTEM (Adams et al., 2010; DiMaio et al., 2013). The splayed open and super splayed open classes were not refined in cisTEM, and the maps from those classes, as well as their FSC curves, were generated by RELION.

**Model Generation, Refinement and Analysis—**The GluN1 homology model was constructed by SWISS-MODEL (Arnold et al., 2006) based on the crystal structure of the GluN1/GluN2B (PDB code: 4PE5) (Karakas and Furukawa, 2014). The GluN2A homology model was based on three sources. The ATD of the GluN2A homology model was based on the crystal structure of the isolated GluN1/GluN2A ATD (Romero-Hernandez et al., 2016) (PDB code: 5TQ0), the D1 lobe of the LBD was based on the crystal structure of the isolated LBD of GluN1/GluN2A (Yi et al., 2016) (PDB code: 5I57), and the remainder of the homology model was based on the cryoEM structure of the GluN1/GluN2A/GluN2B triheteromeric NMDAR (Lu et al., 2017) (PDB code: 5UOW). Each subunit was split into 5 parts (R1, R2, D1, D2, and TMD). The 5 pieces of each subunit (20 in total) were independently rigid-body fitted into each of the cryoEM density maps using UCSF Chimera (Pettersen et al., 2004). The only exceptions to this procedure were the splayed open structure, for which the ATD and LBD dimers of each subunit, as well as the TMD heterotetramers was fitted as a single rigid-body, and the super splayed structures, where each subunit's ATD or LBD heterodimer and TMD tetramer was fitted as a single rigid-body. Each model was then manually inspected and corrected in COOT (Emsley and

Author Manuscript Author Manuscript Author Manuscript Author Manuscript

Cowtan, 2004), followed by real-space refinement in Phenix (Adams et al., 2010). FSC curves correlating the final models to the cryoEM maps were generated in Phenix.

All center of mass calculations are based on the center of mass of the alpha-carbon of the noted residues (Figure S3). In the case of the ATD clamshell closure angles, the alpha carbon of Ser 150 residue was used as the pivot point along with the COMs of R1 and R2 lobes of GluN2A to measure the clamshell angle. The ATD-LBD angle refers to the angle between two vectors, the first of which passes through the COMs of the LBD D1 and D2 lobes, and the second of which passes through COMs of the ATD R1 and R2 lobes. To measure statistical significance, we used two-tailed homoscedastic student's t-tests in Microsoft Excel. In box-plots, colored boxes represent the first and third quartile of each population, and the error bars represent the maximum and minimum values. All the figures were made using UCSF's Chimera and PyMOL (Yuan et al., 2016).

## QUANTIFICATION AND STATISTICAL ANALYSIS

**TEVC and Radiolabeled SPA assay—**The TEVC recordings were performed on three or four biological replicates. Traces were then analyzed by MATLAB to obtain percent Inhibition at each zinc concentration. The data was fit to a single-site binding model to obtain the $IC_{50}$ values. Error bars represent standard error. No values were omitted from analysis for this experiment. For the radiolabeled SPA experiments the counts remaining on the beads at each zinc concentration were fit to a single-exponential curve with an offset, to account for the small fraction of counts which remained bound to the beads. The off-rate vs. zinc concentration was then fit to a single-site binding model using Excel Solver to obtain the $IC_{50}$ value for zinc-inhibition. The data represent three independent replicates, and the error bars represent standard errors. No data points were omitted from the analysis.

**Particle Counts and Population Distribution—**Particles were picked from the motion-corrected and dose-weighted micrographs using gAutomatch (Unpublished: URL http://www.mrc-lmb.cam.ac.uk/kzhang/Gautomatch/) or DoG-Picker (Voss et al., 2009). Relion was used for Reference-free 2D-classification, generally in three rounds using binning factors of 5, 3, and 1. Approximately 30 of the final classes were then selected, for each dataset, as templates for template-based particle picking using gAutomatch. The second dataset was cleaned up using the same approach as above. The final two datasets were then combined, and particles whose center was closer than 90 Å to another particle were removed. This represents the total number of particles for each dataset. After ab-initio model generation, 3D classification was carried out in Relion. The number of particles which belong to each 3D-class after this initial classification was used as the basis for the population of the receptor in that class in Figure 2. Only the splayed-open and the super-splayed classes showed improved resolution by further classification and particle removal.

**Distance Measurements—**All distance measurements represent the center of mass calculation for the alpha-carbon coordinates of the indicated domain (as defined in Figure S3). There are six independent structures in the 2-knuckle-sym conformation, two in the 2-knuckle-asym and Super-splayed conformations, and three in the 1-knuckle and extended conformations. In the representative box plots (Figures 4–6), the bars represent the first and

Author Manuscript Author Manuscript Author Manuscript Author Manuscript

third quartile of each population, and the error bars represent the maximum and minimum values. No structures were omitted from the analysis. For the triNMDAR in the 2-knuckle-asym conformation, where we have one set of map/coordinates with the entire receptor and a higher resolution set focused on the ECD, the measurements were performed using the ECD focused maps/coordinates whenever possible.

## DATA AND SOFTWARE AVAILABILITY

**Data Resources—**The three-dimensional cryo-EM density maps for the diheteromeric GluN1/GluN2A receptor at pH 8.0 in the presence of 100 μM EDTA or 1 μM zinc have been deposited in the EM Database under the accession codes EMDB: EMD-9158 and EMD-9157, respectively, and the coordinates for the structures have been deposited in Protein Data Bank under accession codes PDB: 6MMP and 6MMN. The density maps for the diheteromeric GluN1/GluN2A receptor at pH 7.4 in the 2-knuckle-symmetric conformation in the presence of 1 mM EDTA or 1 mM zinc and 3 mM EDTA have been deposited in the EM Database under the accession codes EMDB: EMD-9150 and EMD-9159, respectively, and the coordinates for the structures have been deposited in Protein Data Bank under accession codes PDB: 6MMG and 6MMR.

The density maps for the diheteromeric GluN1/GluN2A receptor at pH 7.4 in the presence of 1 μM zinc in the 2-knuckle-asymmetric, 1-knuckle, or the extended conformations have been deposited in the EM Database under the accession codes EMDB: EMD-9155, EMD-9154 and EMD-9156, respectively, and the coordinates for the structures have been deposited in Protein Data Bank under accession codes PDB: 6MML, 6MMK and 6MMM. The density maps for the diheteromeric GluN1/GluN2A receptor at pH 7.4 in the presence of 1 mM zinc in the extended-2, splayed-open, or the super-splayed conformations have been deposited in the EM Database under the accession codes EMDB: EMD-9151, EMD-9152 and EMD-9153, respectively, and the coordinates for the structures have been deposited in Protein Data Bank under accession codes PDB: 6MMH, 6MMI and 6MMJ.

The density maps for the diheteromeric GluN1/GluN2A receptor at pH 6.1 in the presence of 1 μM zinc in the 1-knuckle, extended, or the super-splayed conformations have been deposited in the EM Database under the accession codes EMDB: EMD-9147, EMD-9148 and EMD-9149, respectively, and the coordinates for the structures have been deposited in Protein Data Bank under accession codes PDB: 6MM9, 6MMA and 6MMB.

The density maps for the triheteromeric GluN1/GluN2A/GluN2A* receptor at pH 7.4 in the presence of 1 mM EDTA has been deposited in the EM Database under the accession code EMDB: EMD-9160 and the coordinates for the structure has been deposited in Protein Data Bank under accession code PDB: 6MMS. The density maps for the triheteromeric GluN1/GluN2A/GluN2A* receptor at pH 7.4 in the presence of 1 μM zinc in the 2-knuckle-symmetric, 2-knuckle-asymmetric, 1-knuckle, or the extended conformations have been deposited in the EM Database under the accession codes EMDB: EMD-9164, EMD-9162, EMD-9161 and EMD-9165, respectively, and the coordinates for the structures have been deposited in Protein Data Bank under accession codes PDB: 6MMW, 6MMU, 6MMT and 6MMX. For the triheteromeric GluN1/GluN2A/GluN2A* receptor in 1 μM zinc and in the 2-knuckle-asymmetric conformation, the extracellular domain focused-refinement density

Author Manuscript Author Manuscript Author Manuscript Author Manuscript

map and the coordinates have been deposited in the EM Database under the accession code EMDB: EMD-9163 and the Protein Data Bank under accession code PDB: 6MMV, respectively.

## Supplementary Material

Refer to Web version on PubMed Central for supplementary material.

## Acknowledgements

We thank Z.H. Yu, H.T. Chou, and R. Huong from Janelia Research Campus for assistance with data collection. Electron microscopy was performed at Oregon Health and Science University (OHSU) at the Multiscale Microscopy Core (MMC) with technical support from the Oregon Health and Science University (OHSU)-FEI Living Lab and the OHSU Center for Spatial Systems Biomedicine (OCSSB). We thank Richard W. Roberts, Terry T. Takahashi, and Jasmine M. Corbin for providing us with the sequence of the DNSA tag. Elemental analysis to quantitate background zinc contamination was performed in the OHSU Elemental Analysis Core. We thank all of the members of the Gouaux, Baconguis, and Whorton labs for helpful discussions. We thank A.J. Romero and L. Vaskalis for help with the illustrations, and we thank H. Owen, N. Yoder, and V. Navratna for proofreading. F.J.Y. is supported by the NIH (1F32MH115595). S.C. is supported by the Jane Coffin Childs Fund (61–1591). This work was supported by the NIH (R01NS038631). E.G. is an investigator with the Howard Hughes Medical Institute.

## References

Adams PD, Afonine PV, Bunkoczi G, Chen VB, Davis IW, Echols N, Headd JJ, Hung LW, Kapral GJ, Grosse-Kunstleve RW, et al. (2010). PHENIX: a comprehensive Python-based system for macromolecular structure solution. Acta crystallographica Section D, Biological crystallography 66, 213–221. [PubMed: 20124702]

Amico-Ruvio SA, Murthy SE, Smith TP, and Popescu GK (2011). Zinc effects on NMDA receptor gating kinetics. Biophysical journal 100, 1910–1918. [PubMed: 21504727]

Amico-Ruvio SA, Paganelli MA, Myers JM, and Popescu GK (2012). Ifenprodil effects on GluN2B-containing glutamate receptors. Molecular pharmacology 82, 1074–1081. [PubMed: 22936815]

Arnold K, Bordoli L, Kopp J, and Schwede T (2006). The SWISS-MODEL workspace: a web-based environment for protein structure homology modelling. Bioinformatics 22, 195–201. [PubMed: 16301204]

Bashir ZI, Alford S, Davies SN, Randall AD, and Collingridge GL (1991). Long-term potentiation of NMDA receptor-mediated synaptic transmission in the hippocampus. Nature 349, 156–158. [PubMed: 1846031]

Blanke ML, and VanDongen AM (2008). Constitutive activation of the N-methyl-D-aspartate receptor via cleft-spanning disulfide bonds. The Journal of biological chemistry 283, 21519–21529. [PubMed: 18450751]

Choi YB, and Lipton SA (1999). Identification and mechanism of action of two histidine residues underlying high-affinity Zn2+ inhibition of the NMDA receptor. Neuron 23, 171–180. [PubMed: 10402203]

Christine CW, and Choi DW (1990). Effect of zinc on NMDA receptor-mediated channel currents in cortical neurons. The Journal of neuroscience : the official journal of the Society for Neuroscience 10, 108–116. [PubMed: 1688929]

DiMaio F, Echols N, Headd JJ, Terwilliger TC, Adams PD, and Baker D (2013). Improved low-resolution crystallographic refinement with Phenix and Rosetta. Nature methods 10, 1102–1104. [PubMed: 24076763]

Dolino DM, Chatterjee S, MacLean DM, Flatebo C, Bishop LDC, Shaikh SA, Landes CF, and Jayaraman V (2017). The structure-energy landscape of NMDA receptor gating. Nature chemical biology 13, 1232–1238. [PubMed: 28991238]

Emsley P, and Cowtan K (2004). Coot: model-building tools for molecular graphics. Acta crystallographica Section D, Biological crystallography 60, 2126–2132. [PubMed: 15572765]

Author Manuscript Author Manuscript Author Manuscript Author Manuscript

Erreger K, and Traynelis SF (2005). Allosteric interaction between zinc and glutamate binding domains on NR2A causes desensitization of NMDA receptors. The Journal of physiology 569, 381–393. [PubMed: 16166158]

Erreger K, and Traynelis SF (2008). Zinc inhibition of rat NR1/NR2A N-methyl-D-aspartate receptors. The Journal of physiology 586, 763–778. [PubMed: 18048453]

Fayyazuddin A, Villarroel A, Le Goff A, Lerma J, and Neyton J (2000). Four residues of the extracellular N-terminal domain of the NR2A subunit control high-affinity Zn2+ binding to NMDA receptors. Neuron 25, 683–694. [PubMed: 10774735]

Fernandez-Leiro R, and Scheres SHW (2017). A pipeline approach to single-particle processing in RELION. Acta crystallographica Section D, Structural biology 73, 496–502. [PubMed: 28580911]

Gielen M, Le Goff A, Stroebel D, Johnson JW, Neyton J, and Paoletti P (2008). Structural rearrangements of NR1/NR2A NMDA receptors during allosteric inhibition. Neuron 57, 80–93. [PubMed: 18184566]

Gielen M, Siegler Retchless B, Mony L, Johnson JW, and Paoletti P (2009). Mechanism of differential control of NMDA receptor activity by NR2 subunits. Nature 459, 703–707. [PubMed: 19404260]

Goehring A, Lee CH, Wang KH, Michel JC, Claxton DP, Baconguis I, Althoff T, Fischer S, Garcia KC, and Gouaux E (2014). Screening and large-scale expression of membrane proteins in mammalian cells for structural studies. Nature protocols 9, 2574–2585. [PubMed: 25299155]

Grant T, Rohou A, and Grigorieff N (2018). cisTEM, user-friendly software for single-particle image processing. eLife 7.

Hansen KB, Ogden KK, Yuan H, and Traynelis SF (2014). Distinct functional and pharmacological properties of Triheteromeric GluN1/GluN2A/GluN2B NMDA receptors. Neuron 81, 1084–1096. [PubMed: 24607230]

Hatton CJ, and Paoletti P (2005). Modulation of triheteromeric NMDA receptors by N-terminal domain ligands. Neuron 46, 261–274. [PubMed: 15848804]

Heymann JB, Cardone G, Winkler DC, and Steven AC (2008). Computational resources for cryoelectron tomography in Bsoft. Journal of structural biology 161, 232–242. [PubMed: 17869539]

Karakas E, and Furukawa H (2014). Crystal structure of a heterotetrameric NMDA receptor ion channel. Science 344, 992–997. [PubMed: 24876489]

Karakas E, Simorowski N, and Furukawa H (2009). Structure of the zinc-bound amino-terminal domain of the NMDA receptor NR2B subunit. The EMBO journal 28, 3910–3920. [PubMed: 19910922]

Kornhuber J, Mack-Burkhardt F, Kornhuber ME, and Riederer P (1989). [3H]MK-801 binding sites in post-mortem human frontal cortex. European journal of pharmacology 162, 483–490. [PubMed: 2663525]

Lee CH, Lu W, Michel JC, Goehring A, Du J, Song X, and Gouaux E (2014). NMDA receptor structures reveal subunit arrangement and pore architecture. Nature 511, 191–197. [PubMed: 25008524]

Low CM, Zheng F, Lyuboslavsky P, and Traynelis SF (2000). Molecular determinants of coordinated proton and zinc inhibition of N-methyl-D-aspartate NR1/NR2A receptors. Proceedings of the National Academy of Sciences of the United States of America 97, 11062–11067. [PubMed: 10984504]

Lu W, Du J, Goehring A, and Gouaux E (2017). Cryo-EM structures of the triheteromeric NMDA receptor and its allosteric modulation. Science.

Mastronarde DN (2005). Automated electron microscope tomography using robust prediction of specimen movements. Journal of structural biology 152, 36–51. [PubMed: 16182563]

Mony L, Zhu S, Carvalho S, and Paoletti P (2011). Molecular basis of positive allosteric modulation of GluN2B NMDA receptors by polyamines. The EMBO journal 30, 3134–3146. [PubMed: 21685875]

Mott DD, Doherty JJ, Zhang S, Washburn MS, Fendley MJ, Lyuboslavsky P, Traynelis SF, and Dingledine R (1998). Phenylethanolamines inhibit NMDA receptors by enhancing proton inhibition. Nature neuroscience 1, 659–667. [PubMed: 10196581]

Author Manuscript Author Manuscript Author Manuscript Author Manuscript

Nowak L, Bregestovski P, Ascher P, Herbet A, and Prochiantz A (1984). Magnesium gates glutamate-activated channels in mouse central neurones. Nature 307, 462–465. [PubMed: 6320006]

Nozaki C, Vergnano AM, Filliol D, Ouagazzal AM, Le Goff A, Carvalho S, Reiss D, Gaveriaux-Ruff C, Neyton J, Paoletti P, et al. (2011). Zinc alleviates pain through high-affinity binding to the NMDA receptor NR2A subunit. Nature neuroscience 14, 1017–1022. [PubMed: 21725314]

Pahk AJ, and Williams K (1997). Influence of extracellular pH on inhibition by ifenprodil at N-methyl-D-aspartate receptors in Xenopus oocytes. Neuroscience letters 225, 29–32. [PubMed: 9143010]

Paoletti P (2011). Molecular basis of NMDA receptor functional diversity. The European journal of neuroscience 33, 1351–1365. [PubMed: 21395862]

Paoletti P, Ascher P, and Neyton J (1997). High-affinity zinc inhibition of NMDA NR1-NR2A receptors. The Journal of neuroscience : the official journal of the Society for Neuroscience 17, 5711–5725. [PubMed: 9221770]

Paoletti P, Bellone C, and Zhou Q (2013). NMDA receptor subunit diversity: impact on receptor properties, synaptic plasticity and disease. Nature reviews Neuroscience 14, 383–400. [PubMed: 23686171]

Paoletti P, Perin-Dureau F, Fayyazuddin A, Le Goff A, Callebaut I, and Neyton J (2000). Molecular organization of a zinc binding n-terminal modulatory domain in a NMDA receptor subunit. Neuron 28, 911–925. [PubMed: 11163276]

Paoletti P, Vergnano AM, Barbour B, and Casado M (2009). Zinc at glutamatergic synapses. Neuroscience 158, 126–136. [PubMed: 18353558]

Pettersen EF, Goddard TD, Huang CC, Couch GS, Greenblatt DM, Meng EC, and Ferrin TE (2004). UCSF Chimera--a visualization system for exploratory research and analysis. Journal of computational chemistry 25, 1605–1612. [PubMed: 15264254]

Punjani A, Rubinstein JL, Fleet DJ, and Brubaker MA (2017). cryoSPARC: algorithms for rapid unsupervised cryo-EM structure determination. Nature methods 14, 290–296. [PubMed: 28165473]

Qian J, and Noebels JL (2005). Visualization of transmitter release with zinc fluorescence detection at the mouse hippocampal mossy fibre synapse. The Journal of physiology 566, 747–758. [PubMed: 15919713]

Qian J, and Noebels JL (2006). Exocytosis of vesicular zinc reveals persistent depression of neurotransmitter release during metabotropic glutamate receptor long-term depression at the hippocampal CA3-CA1 synapse. The Journal of neuroscience : the official journal of the Society for Neuroscience 26, 6089–6095. [PubMed: 16738253]

Regan MC, Grant T, McDaniel MJ, Karakas E, Zhang J, Traynelis SF, Grigorieff N, and Furukawa H (2018). Structural Mechanism of Functional Modulation by Gene Splicing in NMDA Receptors. Neuron 98, 521–529 e523. [PubMed: 29656875]

Romero-Hernandez A, Simorowski N, Karakas E, and Furukawa H (2016). Molecular Basis for Subtype Specificity and High-Affinity Zinc Inhibition in the GluN1-GluN2A NMDA Receptor Amino-Terminal Domain. Neuron 92, 1324–1336. [PubMed: 27916457]

Scheres SH (2012). RELION: implementation of a Bayesian approach to cryo-EM structure determination. Journal of structural biology 180, 519–530. [PubMed: 23000701]

Scheres SH, and Chen S (2012). Prevention of overfitting in cryo-EM structure determination. Nature methods 9, 853–854. [PubMed: 22842542]

Sensi SL, Paoletti P, Bush AI, and Sekler I (2009). Zinc in the physiology and pathology of the CNS. Nature reviews Neuroscience 10, 780–791. [PubMed: 19826435]

Serraz B, Grand T, and Paoletti P (2016). Altered zinc sensitivity of NMDA receptors harboring clinically-relevant mutations. Neuropharmacology 109, 196–204. [PubMed: 27288002]

Sirrieh RE, MacLean DM, and Jayaraman V (2013). Amino-terminal domain tetramer organization and structural effects of zinc binding in the N-methyl-D-aspartate (NMDA) receptor. The Journal of biological chemistry 288, 22555–22564. [PubMed: 23792960]

Sirrieh RE, MacLean DM, and Jayaraman V (2015). A conserved structural mechanism of NMDA receptor inhibition: A comparison of ifenprodil and zinc. The Journal of general physiology 146, 173–181. [PubMed: 26170175]

Author Manuscript Author Manuscript Author Manuscript Author Manuscript

Song X, Jensen MO, Jogini V, Stein RA, Lee CH, McHaourab HS, Shaw DE, and Gouaux E (2018). Mechanism of NMDA receptor channel block by MK-801 and memantine. Nature.

Tajima N, Karakas E, Grant T, Simorowski N, Diaz-Avalos R, Grigorieff N, and Furukawa H (2016). Activation of NMDA receptors and the mechanism of inhibition by ifenprodil. Nature 534, 63–68. [PubMed: 27135925]

Traynelis SF, Burgess MF, Zheng F, Lyuboslavsky P, and Powers JL (1998). Control of voltage-independent zinc inhibition of NMDA receptors by the NR1 subunit. The Journal of neuroscience : the official journal of the Society for Neuroscience 18, 6163–6175.

Traynelis SF, and Cull-Candy SG (1990). Proton inhibition of N-methyl-D-aspartate receptors in cerebellar neurons. Nature 345, 347–350. [PubMed: 1692970]

Traynelis SF, Wollmuth LP, McBain CJ, Menniti FS, Vance KM, Ogden KK, Hansen KB, Yuan H, Myers SJ, and Dingledine R (2010). Glutamate receptor ion channels: structure, regulation, and function. Pharmacological reviews 62, 405–496. [PubMed: 20716669]

Vergnano AM, Rebola N, Savtchenko LP, Pinheiro PS, Casado M, Kieffer BL, Rusakov DA, Mulle C, and Paoletti P (2014). Zinc dynamics and action at excitatory synapses. Neuron 82, 1101–1114. [PubMed: 24908489]

Voss NR, Yoshioka CK, Radermacher M, Potter CS, and Carragher B (2009). DoG Picker and TiltPicker: software tools to facilitate particle selection in single particle electron microscopy. Journal of structural biology 166, 205–213. [PubMed: 19374019]

Yi F, Mou TC, Dorsett KN, Volkmann RA, Menniti FS, Sprang SR, and Hansen KB (2016). Structural Basis for Negative Allosteric Modulation of GluN2A-Containing NMDA Receptors. Neuron 91, 1316–1329. [PubMed: 27618671]

Yuan H, Myers SJ, Wells G, Nicholson KL, Swanger SA, Lyuboslavsky P, Tahirovic YA, Menaldino DS, Ganesh T, Wilson LJ, et al. (2015). Context-dependent GluN2B-selective inhibitors of NMDA receptor function are neuroprotective with minimal side effects. Neuron 85, 1305–1318. [PubMed: 25728572]

Yuan S, Chan HCS, Filipek S, and Vogel H (2016). PyMOL and Inkscape Bridge the Data and the Data Visualization. Structure 24, 2041–2042. [PubMed: 27926832]

Zhang K (2016). Gctf: Real-time CTF determination and correction. Journal of structural biology 193, 1–12. [PubMed: 26592709]

Zhao Y, Chen S, Yoshioka C, Baconguis I, and Gouaux E (2016). Architecture of fully occupied GluA2 AMPA receptor-TARP complex elucidated by cryo-EM. Nature 536, 108–111. [PubMed: 27368053]

Zheng F, Erreger K, Low CM, Banke T, Lee CJ, Conn PJ, and Traynelis SF (2001). Allosteric interaction between the amino terminal domain and the ligand binding domain of NR2A. Nature neuroscience 4, 894–901. [PubMed: 11528420]

Zheng SQ, Palovcak E, Armache JP, Verba KA, Cheng Y, and Agard DA (2017). MotionCor2: anisotropic correction of beam-induced motion for improved cryo-electron microscopy. Nature methods.

Zhu S, Stein RA, Yoshioka C, Lee CH, Goehring A, McHaourab HS, and Gouaux E (2016). Mechanism of NMDA Receptor Inhibition and Activation. Cell 165, 704–714. [PubMed: 27062927]

Zuo J, De Jager PL, Takahashi KA, Jiang W, Linden DJ, and Heintz N (1997). Neurodegeneration in Lurcher mice caused by mutation in delta2 glutamate receptor gene. Nature 388, 769–773. [PubMed: 9285588]

Author Manuscript Author Manuscript Author Manuscript Author Manuscript

## Highlights

- Cryo-EM structure of the diheteromeric GluN1/GluN2A NMDA receptor
- Receptor populates multiple structural states dependent upon zinc concentration and pH
- Zinc-induced closure of ATD clamshells propagated to LBD layer and to ion channel gate
- Rupture of LBD D1-D1 interface uncouples agonist binding from ion channel gating

Author Manuscript
Author Manuscript
Author Manuscript
Author Manuscript



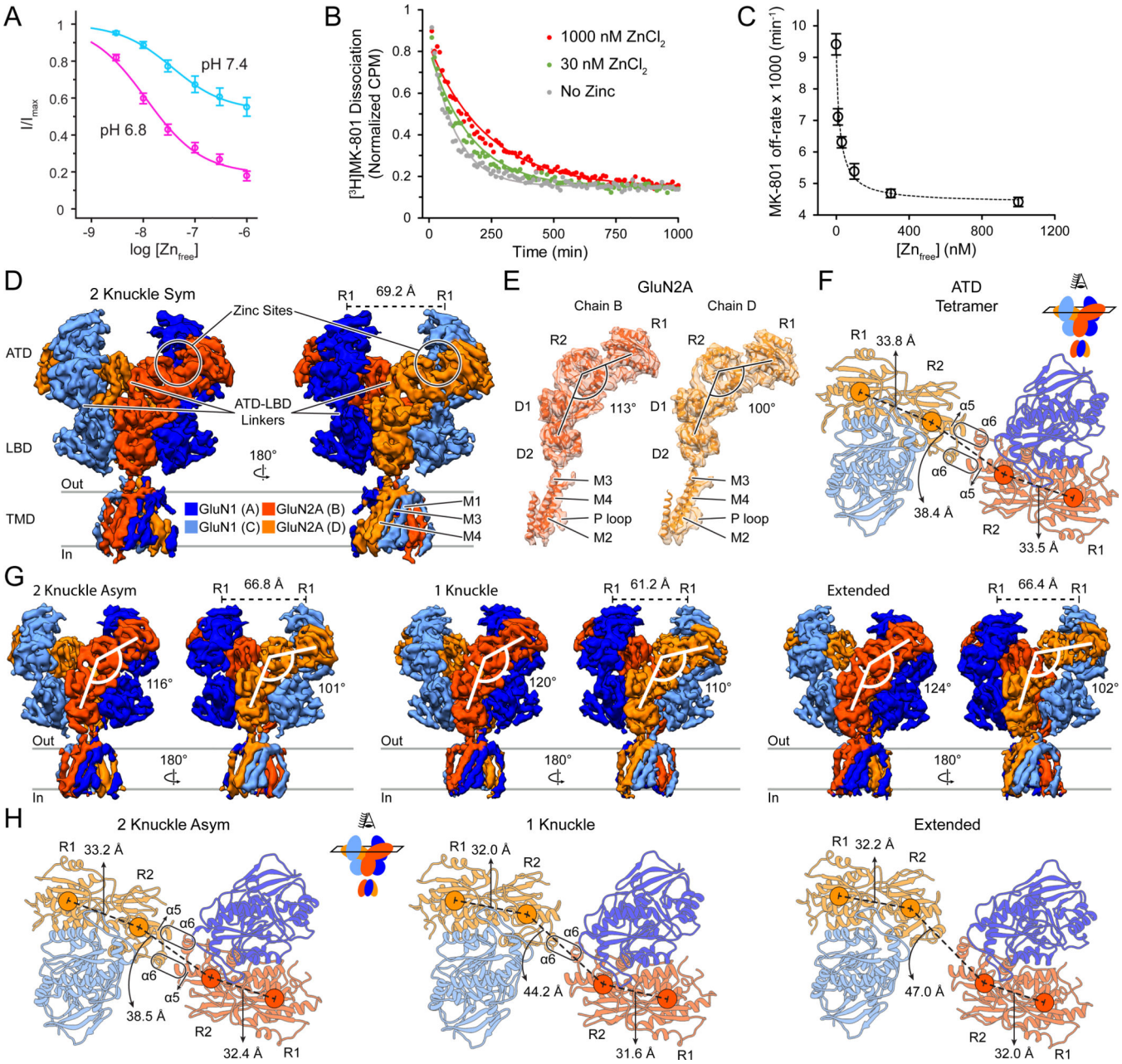


**Figure 1. GluN1/GluN2A Diheteromeric Receptor Activity Modulation by Proton and Zinc, and CryoEM Structures at pH 7.4 in the Absence or Presence of 1 μM Zinc.**

(A) Zinc-inhibition of the GluN1/GluN2A receptor construct at pH 7.4 (cyan, $IC_{50}$ = 36 ± 1 nM) and pH 6.8 (magenta, $IC_{50}$ = 12 ± 1 nM) in the presence of 100 μM glutamate and glycine. $I_{max}$ is obtained by measuring currents in the absence of zinc. Data are mean ± SEM of 3–4 oocytes. See also Figure S1A-B.

(B) Dissociation of [$^3$H]MK-801 from agonist-bound affinity-purified diNMDAR (100 μM glutamate and glycine) in the absence of zinc (grey), in the presence of 30 nM zinc (green), or 1 μM zinc (red). A single-exponential curve (solid lines) is used to obtain the off-rate of MK-801.

Author Manuscript Author Manuscript Author Manuscript Author Manuscript

(C) Off-rate of [$^3$H]MK-801 as a function of zinc at pH 7.4 in the presence of 100 μM glutamate and glycine. Zinc-inhibition $IC_{50}$ = 17.3 ± 1.4 nM based on a one-site binding model. Data are mean ± SEM of three independent replicates.

(D and G) Side views of the diNMDAR cryoEM map in the presence of 1 mM glutamate and glycine at pH 7.4 with 1 mM EDTA (D) or in the presence of 1 μM zinc (G). The distance between the center of mass (COM) of the upper lobes (R1) of GluN1 ATD are shown. See also Figures S2–S4.

(E) Atomic model of each GluN2A subunit fitted into the density map. The ATD-LBD angle is indicated for the two subunits.

(F and H) Top view of the atomic model for the ATD of the diNMDAR in the absence of zinc (F) or in the presence of 1 μM zinc (H). COMs of R1 and R2 lobes for the two GluN2A subunits are shown (circles), with their distance indicated. The rounded rectangles represent the ‘knuckles’ and show the interaction between the α5 and α6 helices of opposing GluN2A subunits for the 2-knuckle conformations, and between α6 and α6 helices for the 1-knuckle conformation.

Author Manuscript Author Manuscript Author Manuscript Author Manuscript

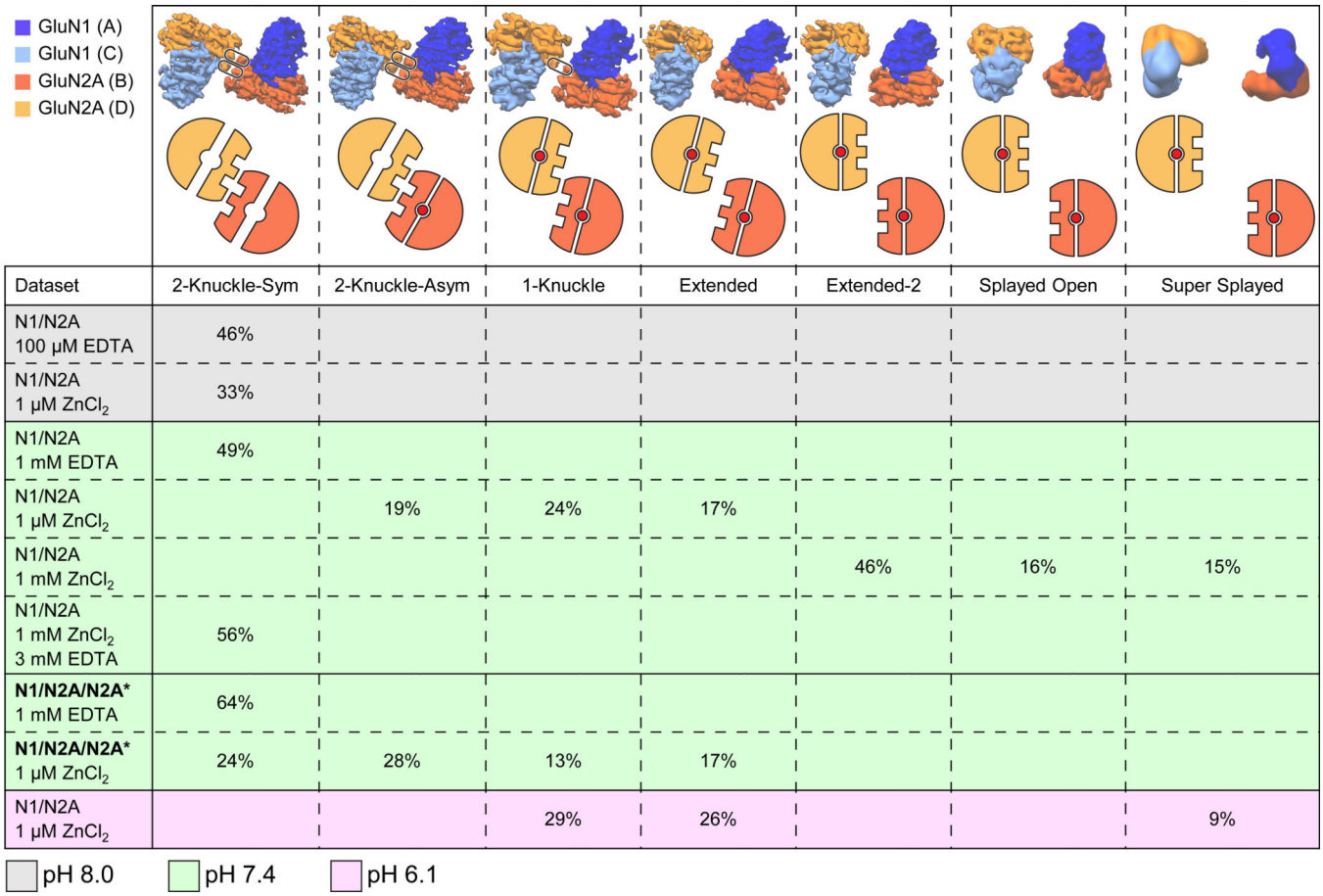


**Figure 2. Population Distribution of the Receptor among Various Conformations**

Proportion of 2D-cleaned up particles distributed into each conformational class depending on the construct used, as well as zinc and proton concentrations. N1/N2A refers to the diheteromeric GluN1/GluN2A receptor. The N1/N2A/N2A* refers to the triheteromeric GluN1/GluN2A/GluN2A* receptor. See also Tables S1–S3

Author Manuscript Author Manuscript Author Manuscript Author Manuscript

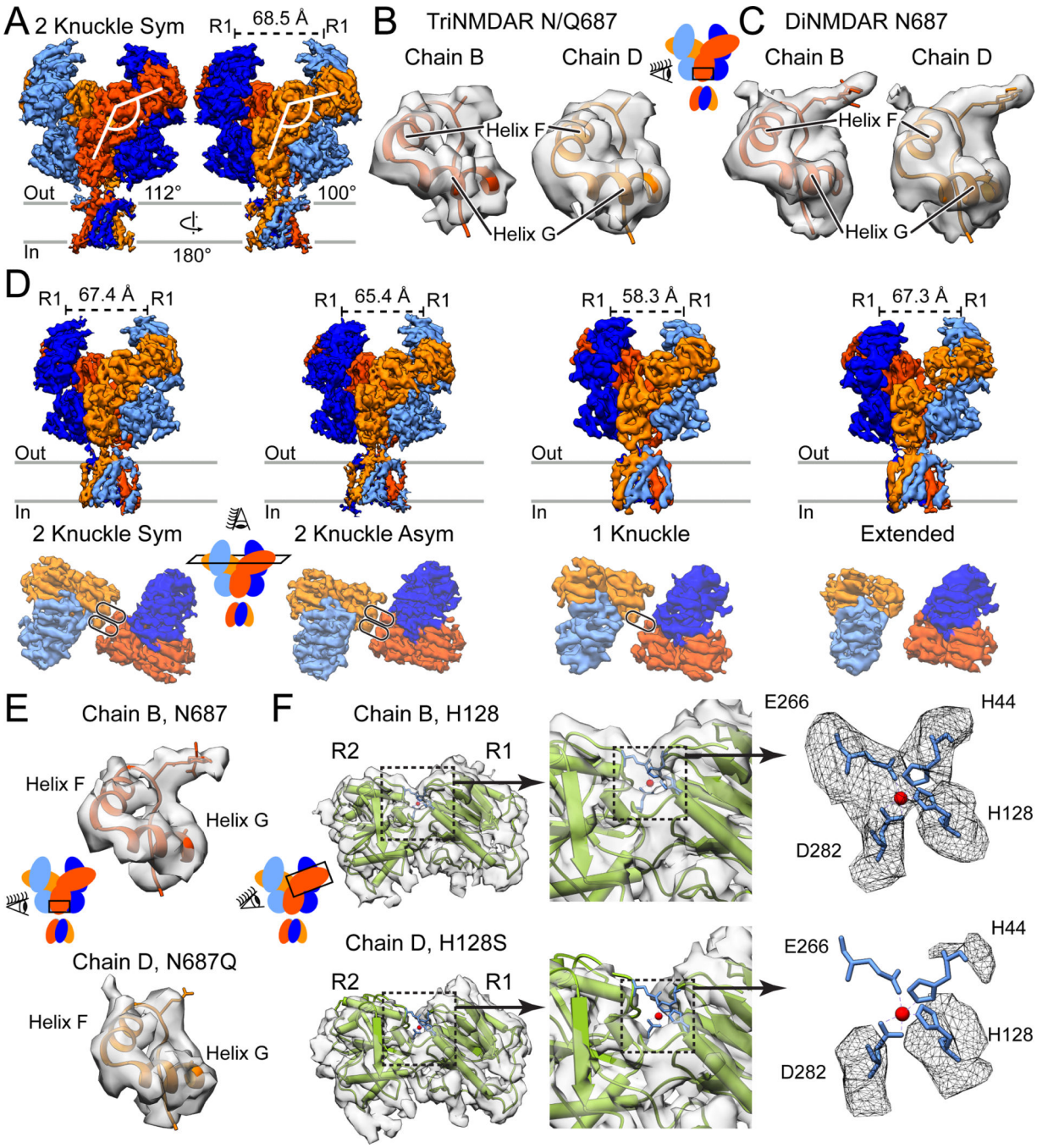


**Figure 3. CryoEM Structures of the GluN1/GluN2A/GluN2A* triNMDAR**

(A) Side views of the GluN1/GluN2A/GluN2A* triNMDAR cryoEM map in the presence of 1 mM glutamate and glycine at pH 7.4 with 1 mM EDTA. The distance between COM of the upper lobes (R1) of GluN1 ATD, as well as the ATD-LBD angle for the two GluN2A subunits, are shown. See also Figure S2.

(B and C) Atomic model and the associated cryoEM density for the GluN2 subunit of the triNMDAR (B) and the diNMDAR (C) in the vicinity of residue 687 in the LBD D2 lobe. There is density consistent with glycosylation of N687 in the diNMDAR, however, this

Author Manuscript Author Manuscript Author Manuscript Author Manuscript

density is not present in either subunit for the triNMDAR. Since distinguishing between GluN2A and GluN2A* subunits is not possible based on glycosylation at residue 687, residue 687 in the map is represented as an alanine.

(D) Side view of the full receptor (top) and top view of the ATD (bottom) of the GluN1/GluN2A/GluN2A* triNMDAR cryoEM map in the presence of 1 mM glutamate and glycine and 1 μM zinc at pH 7.4. See also Figures S1 and S5.

(E) Atomic model and the associated map for the GluN2A subunit (Chain B, top) and the GluN2A* subunit (Chain D, bottom) in the vicinity of residue 687 for the triNMDAR 2-knuckle-asym conformation in the presence of 1 μM zinc. At the same contour level, there is density consistent with glycosylation at only one GluN2 subunit, allowing for the identification of the wt GluN2A and the H128S & N687Q mutant GluN2A* subunits.

(F) The crystal structure of the GluN2A ATD bound by zinc (PDB: 5TPW) fitted into the cryoEM map of the two GluN2 subunits of the triNMDAR 2-knuckle-asym conformation with the R1 lobes aligned. There is density consistent with four amino acid sidechains (H44, H128, E266, D282) coordinating zinc for the WT-subunit. At the same contour level, there is no density in the vicinity of the zinc-binding pocket for the GluN2A* subunit with the H128S mutation.

Author Manuscript Author Manuscript Author Manuscript Author Manuscript

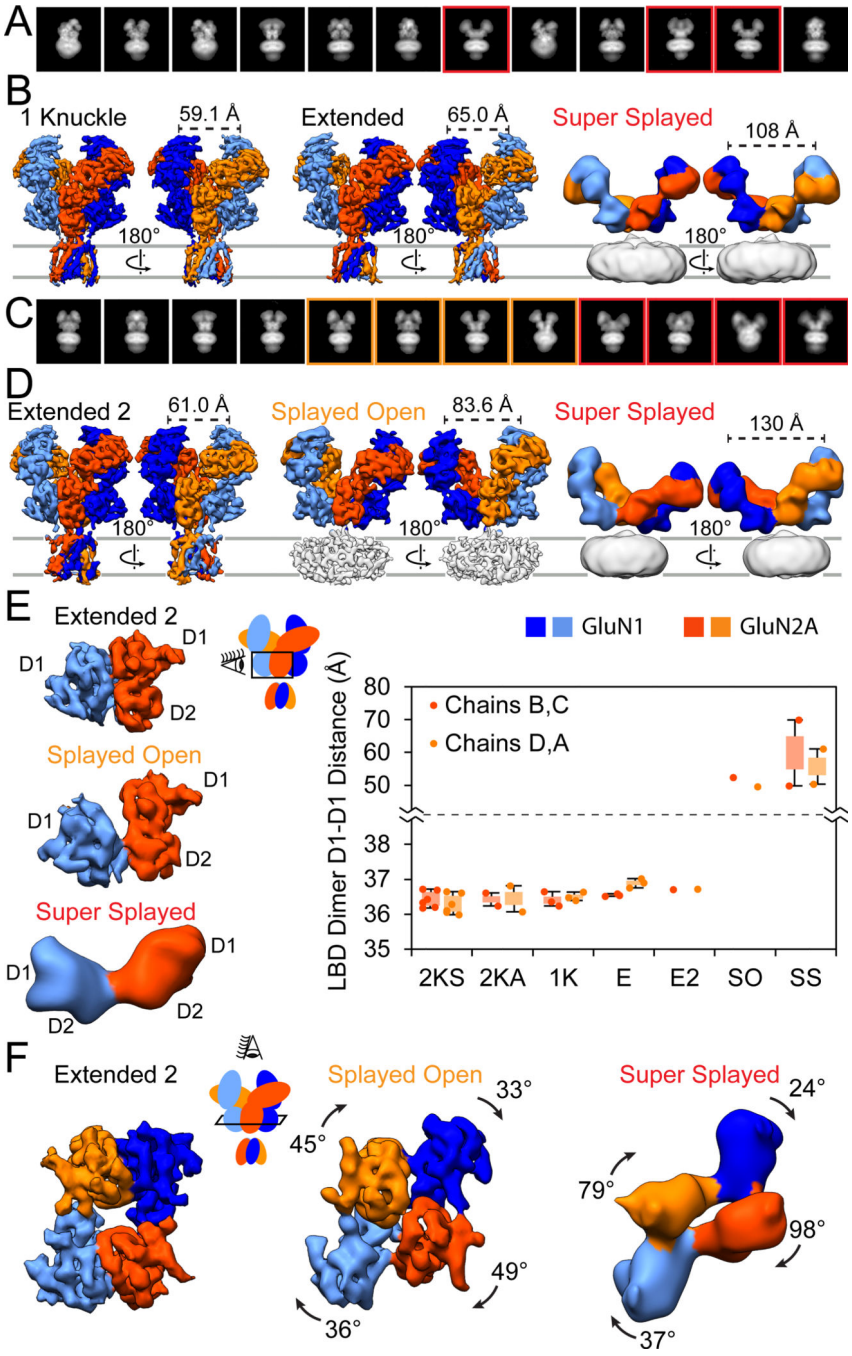


**Figure 4. CryoEM Structures of the GluN1/GluN2A diNMDAR in High Concentrations of Proton and Zinc.**

(A) Representative 2D class averages of the diNMDAR in the presence of 1 mM glutamate and glycine and 1 μM zinc at pH 6.1, with red boxes outlining the supersplayed conformation.

(B) Side views of the diNMDAR cryoEM map in the presence of 1 mM glutamate and glycine and 1 μM zinc at pH 6.1. See also Figure S6.

Author Manuscript Author Manuscript Author Manuscript Author Manuscript

(C) Representative 2D class averages of the diNMDAR in the presence of 1 mM glutamate and glycine and 1 mM zinc at pH 7.4, with orange and red boxes outlining the splayed and the super-splayed conformations, respectively.
(D) Side views of the diNMDAR cryoEM map in the presence of 1 mM glutamate and glycine and 1 mM zinc at pH 7.4. See also Figure S7.
(E) The intact LBD heterodimer of the extended-2 conformation (top) breaking apart in the splayed (middle) and the super-splayed (bottom) conformations, with the GluN1 and GluN2A D1 lobes losing their interactions. The graph on the right shows the distance between the COM of the D1 lobe of GluN1 to the D1 lobe of GluN2A at the major interface for the seven structural classes (2KS = 2-knuckle-sym, 2KA = 2-knuckle-asym, 1K = 1-knuckle, E = extended, E2 = extended-2, SO = splayed-open, SS = super-splayed). Bars represent the first and third quartile of each population, and the error bars represent the maximum and minimum values.
(F) Top view of the LBD for the structures in (D). There is a clockwise rotation for each subunit's LBD when the D1-D1 interface is broken in the splayed-open or super-splayed conformations as compared to the extended-2 conformation.

Author Manuscript Author Manuscript Author Manuscript Author Manuscript

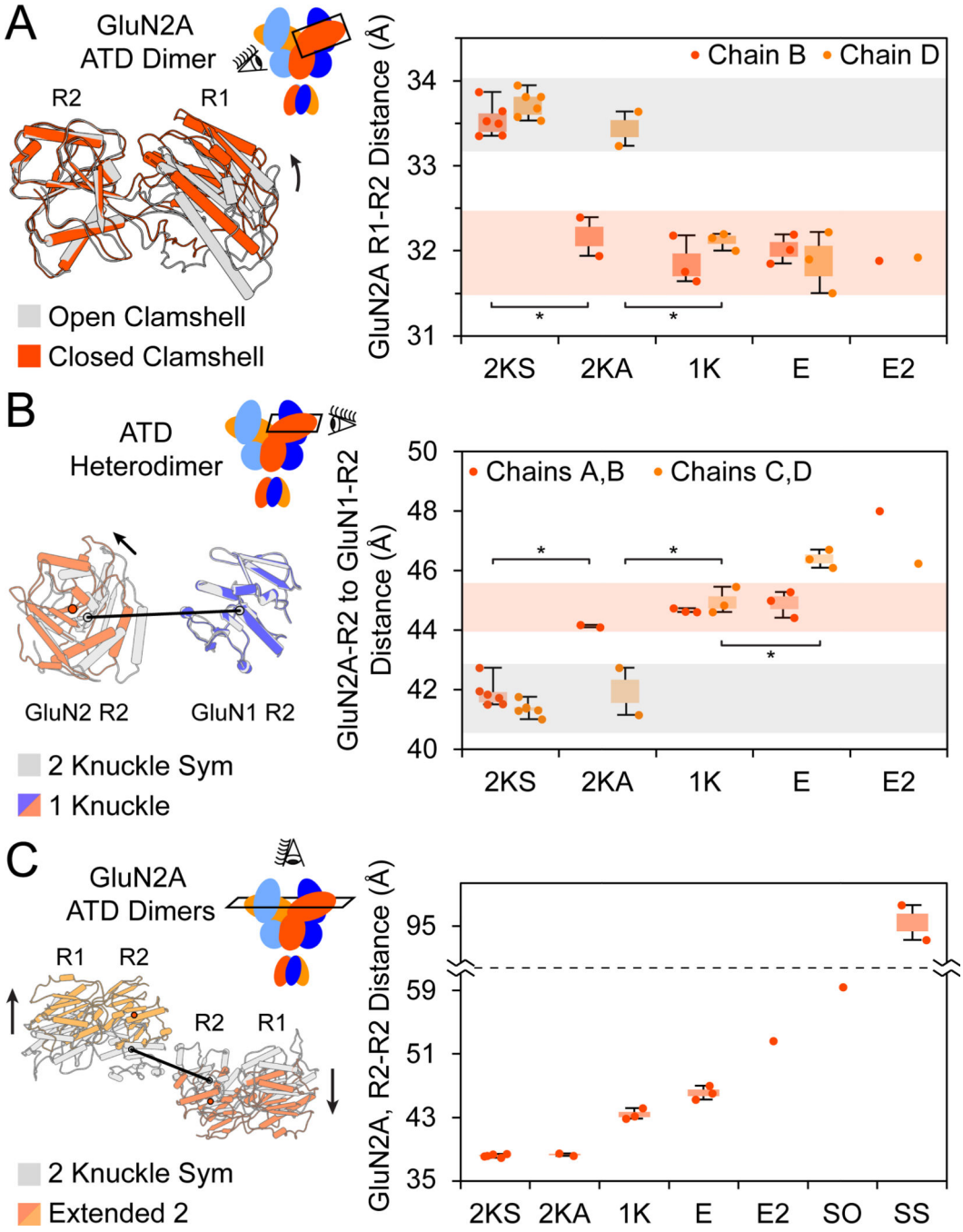


**Figure 5. Zinc-Induced Conformational Rearrangements at the ATD**

(A) Distance between COMs of the R1 and R2 lobes of GluN2A subunits for the various structural classes. The area shaded in grey represents the open ATD clamshell, and the area shaded in red represents the closed ATD clamshell. The extended-2, splayed-open and super-splayed conformations were not included in this analysis due to poor resolution. Side view of the GluN2A ATD in the closed and open clamshell conformations is shown to the right, with the R2 lobes aligned. The black arrow indicates the direction of motion. * denotes significance ($p < 0.05$) using a two-tailed homoscedastic student's t-tests.

Author Manuscript Author Manuscript Author Manuscript Author Manuscript

(B) Closure of the ATD clamshell increases the distance between the GluN1 and GluN2A R2 lobes. The grey shaded area represents the open GluN2A ATD clamshell, and the red shaded area represents the closed GluN2A ATD clamshells with well-defined density for ATD-LBD linkers. Side view of the GluN1 and GluN2A R2 lobes in the closed and open GluN2A clamshell conformations is shown to the right, with the R2 lobes of GluN1 aligned. (C) When both ATD clamshells are closed, the GluN2A R2 lobes move away from each other perpendicular to the R1-R2 axis. Top view of the GluN2A ATDs in the 2-knuckle and extended-2 conformations is shown to the right, aligned by the pseudo-symmetry axes. The black arrows indicates the direction of motion.

Author Manuscript Author Manuscript Author Manuscript Author Manuscript

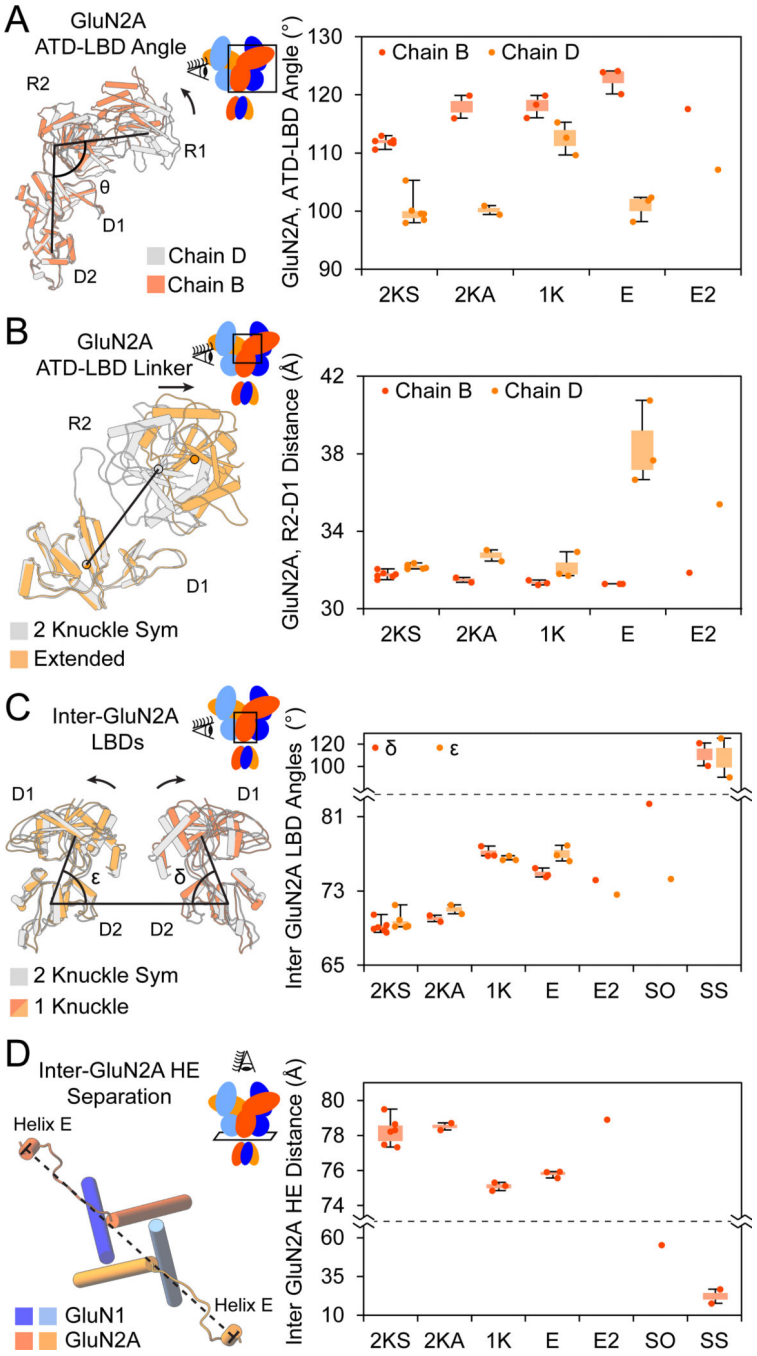


**Figure 6. Translation of Conformation Changes from ATD to the LBD and the Gate**

(A) The ATD-LBD angles for the seven structural classes show conformational differences between the two GluN2A subunits, breaking C2-symmetry. Side view of the GluN2A ECD for chains B and D of the 2-knuckle-asym conformation is shown to the right, with the LBD aligned.

(B) The distance between the lower lobe of the ATD and the upper lobe of the LBD for GluN2A. An asymmetry exists between the two GluN2A subunits with respect to the ATD-LBD distance, with this distance being consistently higher for chain D than chain B. This

Author Manuscript Author Manuscript Author Manuscript Author Manuscript

distance most dramatically changes for the E and E2 conformations. A side view of the two lobes for chains D of the 2-knuckle-sym and extended conformations is shown to the right, with the D1 lobes aligned. The black arrow indicates the direction of motion.
(C) Inter-GluN2A LBD angles increase during zinc-inhibition. δ and ε are the angles between the vector passing through the COMs of the D2 lobes of GluN2A and vectors passing through the COMs of the D1 and D2 lobes of chains B and D, respectively. Side view of the GluN2A LBD of the 2-knuckle-sym and 1-knuckle conformations is shown to the right, with the pseudo-symmetry axes aligned.
(D) Distance between opposing GluN2A helix E (HE) COMs. Top view of the M3 helix bundle, GluN2A HEs, and the linkers which connect the two are shown to the right.

Author Manuscript Author Manuscript Author Manuscript Author Manuscript

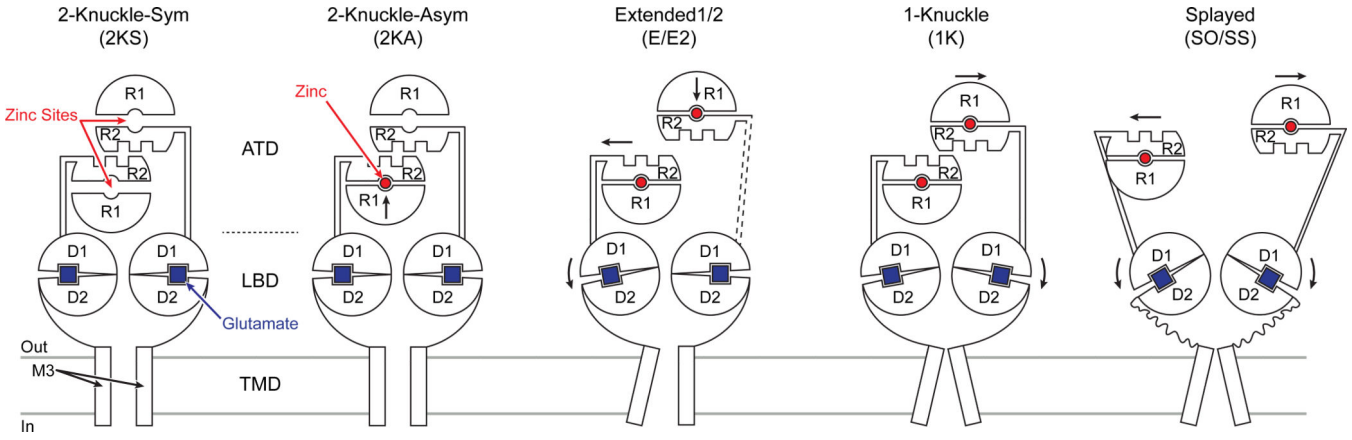


**Figure 7. Schematic Summary for Zinc and Proton-Inhibition of GluN2A Containing NMDARs.**

The schematics for the conformational changes in GluN2A subunits which lead from high $P_O$ conformations (2KS/2KA) to lower $P_O$ states (E-E2) and finally to states with $P_O$ close to zero (1K/SO/SS). These changes originate from the closure of both ATD clamshells in the presence of zinc and protons, leading to the rocking of the LBD clamshells, bringing the lower LBD lobes closer together, and releasing the tension on the gate. In the extended or extended-2 conformations, where one ATD heterodimer has lost interaction with the rest of the receptor, zinc and proton inhibition is not transduced efficiently through the LBD, leading to higher $P_O$ as compared to the 1knuckle state.